



HAL
open science

The Origins of Long-Term Variability in Martian Upper Atmospheric Densities

Xiaohua Fang, Jeffrey M. Forbes, Mehdi Benna, Luca Montabone, Shannon Curry, Bruce Jakosky

► **To cite this version:**

Xiaohua Fang, Jeffrey M. Forbes, Mehdi Benna, Luca Montabone, Shannon Curry, et al.. The Origins of Long-Term Variability in Martian Upper Atmospheric Densities. *Journal of Geophysical Research Space Physics*, 2022, 127, 10.1029/2021JA030145 . insu-03726914

HAL Id: insu-03726914

<https://insu.hal.science/insu-03726914>

Submitted on 16 Mar 2023

HAL is a multi-disciplinary open access archive for the deposit and dissemination of scientific research documents, whether they are published or not. The documents may come from teaching and research institutions in France or abroad, or from public or private research centers.

L'archive ouverte pluridisciplinaire **HAL**, est destinée au dépôt et à la diffusion de documents scientifiques de niveau recherche, publiés ou non, émanant des établissements d'enseignement et de recherche français ou étrangers, des laboratoires publics ou privés.

Copyright

JGR Space Physics

RESEARCH ARTICLE

10.1029/2021JA030145

Key Points:

- Orbital and solar extreme ultraviolet (EUV) effects on CO₂, N₂, Ar, and O densities within 180–275 km are quantified for the first time in Mars Atmosphere and Volatile Evolution (MAVEN) measurements
- Orbital (solar EUV) effect decreases (increases) with altitude, reflecting indirect (direct) control of the upper atmosphere by solar infrared (IR)
- Near 400 km the orbital effect is a key driver, and from solar min to solar max the solar EUV effect changes from secondary to primary

Supporting Information:

Supporting Information may be found in the online version of this article.

Correspondence to:

X. Fang,
Xiaohua.Fang@lasp.colorado.edu

Citation:

Fang, X., Forbes, J. M., Benna, M., Montabone, L., Curry, S., & Jakosky, B. (2022). The origins of long-term variability in Martian upper atmospheric densities. *Journal of Geophysical Research: Space Physics*, 127, e2021JA030145. <https://doi.org/10.1029/2021JA030145>

Received 19 NOV 2021

Accepted 7 MAR 2022

The Origins of Long-Term Variability in Martian Upper Atmospheric Densities

Xiaohua Fang¹ , Jeffrey M. Forbes² , Mehdi Benna^{3,4} , Luca Montabone^{5,6} , Shannon Curry⁷ , and Bruce Jakosky¹ 

¹Laboratory for Atmospheric and Space Physics, University of Colorado, Boulder, CO, USA, ²Ann and H.J. Smead Department of Aerospace Engineering Sciences, University of Colorado, Boulder, CO, USA, ³Center for Space Sciences and Technology, University of Maryland, Baltimore County, Baltimore, MD, USA, ⁴Center for Research and Exploration in Space Science and Technology, NASA Goddard Space Flight Center, Greenbelt, MD, USA, ⁵Space Science Institute, Boulder, CO, USA, ⁶Laboratoire de Météorologie Dynamique/IPSL, Sorbonne Université, Paris, France, ⁷Space Sciences Laboratory, University of California, Berkeley, CA, USA

Abstract We quantify and interpret the long-term variability of dayside Martian upper thermosphere and lower exosphere densities within 180–275 km altitudes. Atmospheric CO₂, N₂, O, and Ar densities are from NASA Mars Atmosphere and Volatile Evolution (MAVEN) observations during the time period of 2015–2020 near solar minimum. These neutral measurements, together with contemporaneous solar irradiance measurements at Mars, enable disentanglement of the orbital effect (due to the annual Sun–Mars distance change with solar longitude) and the solar extreme ultraviolet (EUV) effect in atmospheric density variations. The relative importance of these two effects, which is obtained using a statistical method of Dominance Analysis, reveals the competition between the indirect effect of solar infrared (via the upward coupling from the middle atmosphere) and the direct effect of solar EUV (due to local heating). Our results show that, unlike the orbital effect which is relatively constant at low altitudes and then decreases with increasing altitude, the solar EUV effect nearly monotonically increases. These two effects are comparable at high altitudes (about 240/270/205 km for CO₂/N₂/O). This analysis is extended to include long-term exospheric mass density estimates near 400 km from Mars Global Surveyor and Mars Odyssey data, with a focus on representative solar cycle phases of solar minimum and maximum. It is found that near 400 km, the orbital effect is always a key driver regardless of the solar cycle phase, while the solar EUV effect plays a minor role during solar minimum and is greatly enhanced and slightly exceeds the orbital effect during solar maximum.

Plain Language Summary Observations of the Martian upper atmosphere, which is above ~100 km altitude and is an important intermediate region between the lower and middle atmospheres below and the space environment above, have been especially scarce. Analyses of neutral density distributions in this region are critical for understanding the long-term leakage of Mars' atmosphere into space. This paper is the first to analyze long-term variations of specific atmospheric chemicals (CO₂, N₂, O, and Ar) within 180–275 km altitudes in Mars' atmosphere using measurements by the NASA Mars Atmosphere and Volatile Evolution mission. It is found that most of the long-term variability in upper atmosphere densities are accounted for by heating due to local absorption of solar extreme ultraviolet (EUV) radiation, and by absorption of solar infrared (IR) radiation in the middle atmosphere which then exerts its influence on the overlying upper atmosphere. Long-term variability in IR radiation and its associated effects are driven by Mars' eccentric (non-circular) orbit around the Sun, whereas variability in EUV radiation reaching the planet originates in part at the Sun and is also subject to the orbital effect. The relative importance of these two effects is further partitioned, clearly showing their altitude and solar cycle dependences.

1. Introduction

The processes controlling the long-term variability of the Martian upper atmosphere, which includes the thermosphere and exosphere spanning altitudes above ~100 km, are not fully understood yet are crucial to understanding the climate evolution of Mars and implications for Earth (e.g., Jakosky et al., 2018). As an intermediate region between the lower and middle atmospheres below and the space environment above, the upper atmosphere is driven by the upward coupling from the underlying atmospheric regions and is also subject to the direct control by downward-directed solar radiation. The former influences include atmospheric expansion and contraction

due to solar infrared (IR) and dust aerosol heating, as well as momentum exchange and energy dissipation of upward propagating tides and gravity waves. The latter processes come into play as the upper atmosphere is heated by solar radiation dominantly at extreme ultraviolet (EUV) wavelengths. The upper atmosphere can serve as an informative setting for testing our understanding of mass and energy transport and exchange throughout the atmospheric system. On the other hand, a comprehensive understanding of the upper atmospheric density distribution and its variability is especially desirable from a technical application point of view; for example, it is critical for the planning of aerobraking maneuvers of orbiters and for the prediction of orbital decay from atmospheric drag.

The composition of the Martian upper atmosphere was first measured in 1976 by neutral mass spectrometers onboard the Viking landers VL1 and VL2, from which two altitude profiles (~120–200 km) were obtained along their descent tracks (Nier & McElroy, 1976). Schofield et al. (1997) reported the accelerometer-inferred altitude profile of total mass density during the descent of Mars Pathfinder through the atmosphere below 160 km. Upper atmospheric mass densities have also been derived using accelerometer measurements during aerobraking operations of several spacecraft, including Mars Global Surveyor (MGS) during its phase-1 and phase-2 aerobraking within the altitudes of ~110–160 km (Keating et al., 1998; Wilson, 2002), Mars Odyssey (MO) within ~100–160 km (Tolson et al., 2005), Mars Reconnaissance Orbiter (MRO) within ~100–160 km (Tolson et al., 2008), and Trace Gas Orbiter (TGO) within ~101–120 km (Siddle et al., 2021). Another technique termed Precise Orbit Determination (POD) has been applied to derive exospheric mass densities at ~390 km using MGS data (Forbes et al., 2008) and at ~405 km using MO data (Bruinsma et al., 2014). It is worth noting that both techniques of using accelerometer and POD data yield only total mass densities of the upper atmosphere but no specifics of compositions. In addition, remote sensing observations provide a valuable complement to in-situ measurements. Forget et al. (2009) retrieved upper atmospheric CO₂ altitude profiles (~60–130 km) using stellar occultation observations of Mars Express (MEX).

The Mars Atmosphere and Volatile Evolution (MAVEN) mission (Jakosky et al., 2015) has greatly improved the observation of the upper atmosphere. Its accelerometer data have been used to derive mass density structures near periapsis altitudes of ~140–180 km and occasionally down to ~115–135 km in six deep dip campaigns (Zurek et al., 2017). The limb scan observations of the MAVEN Imaging Ultraviolet Spectrograph (IUVS) instrument have been used to retrieve CO₂ and N₂ densities at 140 km (Yoshida et al., 2020). The temporal and altitude coverage of these data sets is summarized in the bottom panel of Figure 1. It is readily seen that there is a critical observational gap in the upper atmospheric composition and structure within the altitude range of ~200–400 km. Since the Mars orbit insertion of MAVEN in September 2014, its Neutral Gas and Ion Mass Spectrometer (NGIMS) instrument has continuously sampled the upper atmosphere during its periapsis passages (Mahaffy, Benna, Elrod, et al., 2015). MAVEN had a nominal periapsis altitude of 150 km, which was gradually elevated to ~180 km in 2020 to facilitate a relay support for the Mars 2020 mission. The amount of MAVEN NGIMS data accumulated inside this important atmospheric region provides an unprecedented opportunity to investigate the variability of upper atmospheric densities, including long-term variations and trends, which is the primary focus of this work.

Long-term observations of the upper atmosphere are invaluable in not only providing climatological characteristics and variability, but also allowing us to probe the underlying physics by disentangling the primary drivers therein. In order to retrieve seasonal and interannual variabilities, more than two Martian years (MYs) of data are needed. As demonstrated in Figure 1e, long-term data sets have been lacking and it is not surprising that only a handful of long-term data analyses are available in the literature. Forbes et al. (2008) and Krasnopolsky (2010) used over six Earth-years of MGS POD data at ~390 km (marked with “6” in Figure 1e) to empirically derive the dependence of the exospheric mass density on season and solar EUV. Bruinsma et al. (2014) scaled the MGS data to 405 km and then combined with the MO POD data (marked with “9”) to get a solar cycle's worth of data, from which the seasonal and solar flux dependences were empirically estimated. In this study, we analyze about three MYs of MAVEN neutral composition measurements to quantify upper thermosphere and lower exosphere variability at intra-solar cycle time scales. Furthermore, we will make use of the altitude difference between the MAVEN data and the MGS and MO data to investigate vertical variations of the long-term variability in different layers of the upper atmosphere.

We also include in Figure 1 solar conditions for the contextual information of the existing upper atmospheric observations at Mars. Figure 1a presents the time series of sunspot numbers during the last two solar cycles. Figure 1b shows the Sun-Mars distance (r_{SM}), which varies with the solar longitude (L_s , a measure of the season

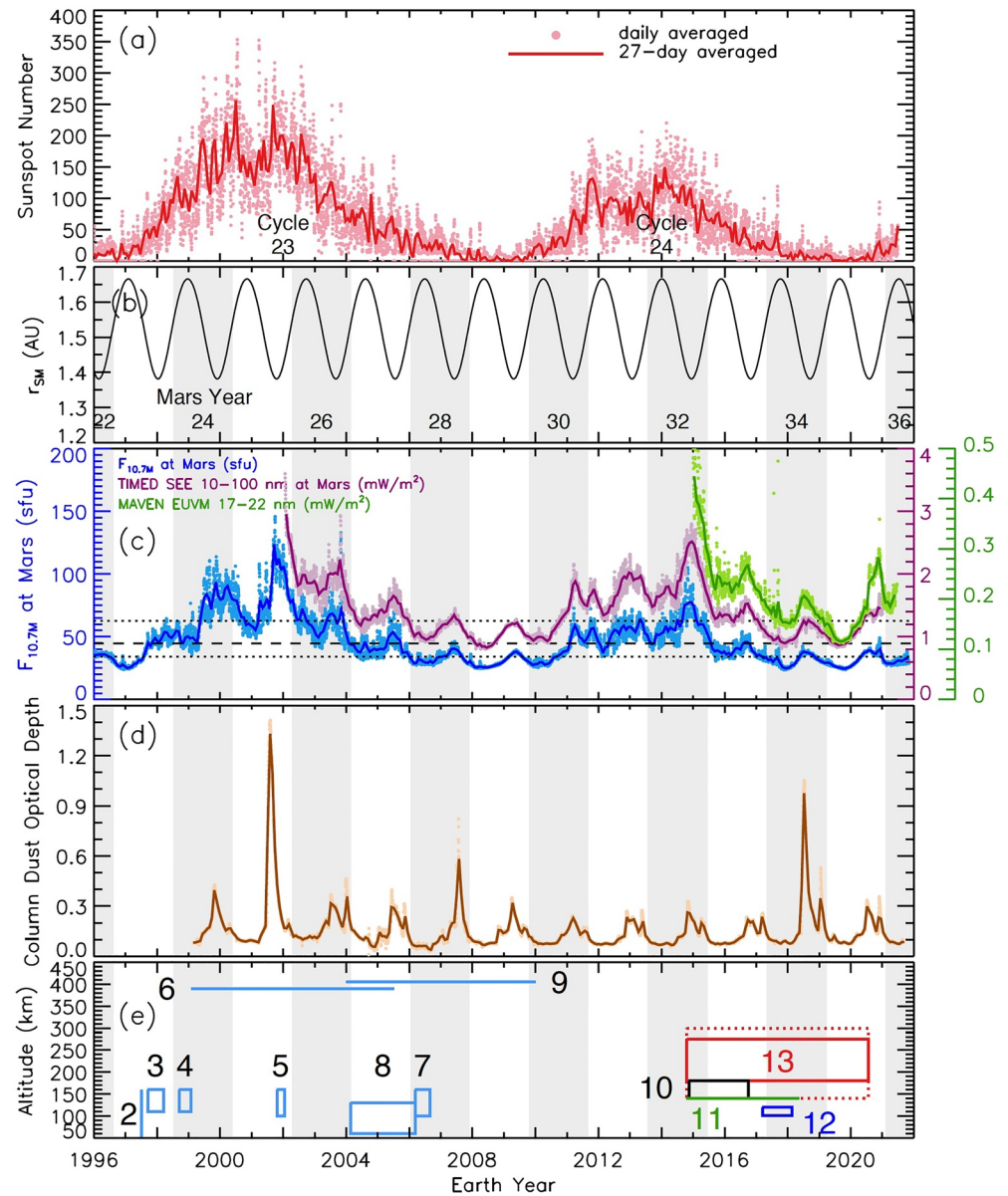


Figure 1. Long-term variability of solar activity and atmospheric dust loading at Mars. Panel (a) presents sunspot numbers during the last two solar cycles. Daily values and 27-day averages are shown by dots and solid lines, respectively, in this panel and also in panels (c) and (d). Panel (b) shows the annual variation of the Sun-Mars distance. Martian years are marked using alternating gray and white shadings. Panel (c) shows the extrapolated $F_{10.7M}$ index at Mars (blue, left axis), solar radiation 10–100 nm fluxes by Thermosphere-Ionosphere-Mesosphere Energetics and Dynamics (TIMED)/Solar EUV Experiment (SEE) after being extrapolated to Mars (purple, right axis) and Mars Atmosphere and Volatile Evolution (MAVEN)/EUV Monitor (EUVM) measured 17–22 nm fluxes (green, right axis). The horizontal dashed line marks the median value of $F_{10.7M}$ (44.5 sfu), and the two dotted lines mark the 25th and 75th percentiles, $F_{10.7M} = 33.9$ and 62.8 sfu, respectively. Panel (d) shows the globally averaged column dust optical depth at $9.3 \mu\text{m}$, scaled to atmospheric pressure of 610 Pa. Panel (e) marks the temporal and altitude coverage of available data sets of upper atmospheric densities (see text): 1, Viking 1 & 2, descent, in-situ (Nier & McElroy, 1976); This data set is outside of the time range and is not shown here, but can be seen in Figure S1 of the Supporting Information S1. 2, Mars Pathfinder, descent, accelerometer (Schofield et al., 1997); 3, Mars Global Surveyor (MGS), aerobraking phase-1, accelerometer (Keating et al., 1998); 4, MGS, aerobraking phase-2, accelerometer (Wilson, 2002); 5, Mars Odyssey (MO), aerobraking, accelerometer (Tolson et al., 2005); 6, MGS, Precise Orbit Determination (POD) (Forbes et al., 2008); 7, MRO, aerobraking, accelerometer (Tolson et al., 2008); 8, Mars Express, stellar occultation (Forget et al., 2009); 9, MO, POD (Bruinsma et al., 2014); 10, MAVEN, accelerometer (Zurek et al., 2017); 11, MAVEN, IUVS limb scan (Yoshida et al., 2020); 12, Trace Gas Orbiter, aerobraking, accelerometer (Siddle et al., 2021); 13, MAVEN, NGIMS in-situ data (dotted box indicating nominal altitude coverage, solid box indicating actual altitude range of our long-term variability study).

on Mars) and repeats itself from one MY to another. Figure 1c shows the solar radiation at the top of the Martian atmosphere, which is characterized by three proxies for intercomparison. One is solar EUV directly measured by the MAVEN EUV Monitor (EUVM, Eparvier et al., 2015), which, however, is available over a limited EUV wavelength range of 17–22 nm (channel A of the instrument). There are two other channels in EUVM, which cover non-EUV in the 0.1–7 nm and 121–122 nm wavelength ranges and thus are of no relevance in this work. Another proxy is the 10.7 cm solar radio flux $F_{10.7M}$, where the subscript “M” indicates that the $F_{10.7}$ index at Earth has been extrapolated to Mars by considering the flux attenuation from 1 AU to r_{SM} and the time shift due to the Earth-Sun-Mars angle (Fang et al., 2017). Daily $F_{10.7M}$ values range between 23.6 and 162.2 solar flux unit (1 sfu = 10^{-22} W/m²/Hz), showing an intensity of 33.9, 44.5, and 62.8 sfu at the 25th, 50th, and 75th percentiles, respectively. The other solar flux proxy is the 10–100 nm integrated irradiance (L3 data) from the Solar EUV Experiment (SEE) onboard the Thermosphere-Ionosphere-Mesosphere Energetics and Dynamics (TIMED) satellite (Woods et al., 2005), which has been similarly scaled from Earth to Mars.

It is illustrated in Figure 1 that a majority of existing upper atmospheric observations (including those by MAVEN) were made during solar minimum or moderate conditions, except for the data sets marked with ‘5’ and ‘6’ in Figure 1e. That is, observations of the Martian upper atmosphere are most abundant at times of low solar activity, as the $F_{10.7M}$ index at Mars largely fell below the median level of 44.5 sfu (Figure 1c). A comparison of MAVEN observations with the other solar minimum data sets (at different altitudes, particularly near 400 km) therefore enables the exploration of vertical variations in the upper atmosphere under comparable solar radiation conditions. In this work, in addition to deriving empirical functions to characterize climatological variations of upper atmospheric densities, we will make a further effort to quantify the relative importance of the orbital effect (due to the annual Sun-Mars distance change) and the solar EUV effect in driving atmospheric density perturbations. We will also extend the relative importance analysis to the long-term MGS and MO POD data sets at ~400 km. By this means, we will evaluate the competition between the orbital and solar EUV effects, not only with altitude during low solar activity but also near 400 km altitude from solar minimum to solar maximum.

2. Data for Upper Atmospheric Densities and Driving Factors

The primary data sets for our long-term variability analysis are in-situ measurements of neutral species by the NGIMS instrument during MAVEN's periapsis passages. MAVEN has been continuously operating in the science mode along elliptical orbits since November 2014. Prior to an aerobraking campaign in early 2019, MAVEN had an orbital period of ~4.5 hr, with its nominal periapsis at ~150 km altitude and apoapsis at ~6,200 km. There were nine short deep-dip campaigns, during which the periapsis was temporarily reduced to as low as ~120 km. After the 2019 aerobraking, MAVEN has been gradually adjusted to a period of ~3.6 hr, with its periapsis and apoapsis near ~180 km and ~4,400 km, respectively. NGIMS is a quadrupole mass spectrometer onboard MAVEN designed to measure neutral and ion species in the Martian upper atmosphere between 1.5 and 150 amu (Mahaffy, Benna, King, et al., 2015). In this study, we focus on major atmospheric neutral species of CO₂, N₂, O, and Ar, and utilize only the NGIMS verified measurements during the inbound segments of the orbits (with a quality flag of ‘IV’). Exclusion of outbound data is to avoid potential adhesive contamination inside the instrument. In this work, we use NGIMS L2, version 8, revision 1 data products that are published on the Planetary Data System (PDS). Considering that the PDS data products become revision 2 after 21 July 2020, we take a conservative approach by limiting our data selection to the time before that, which is long enough to capture the variability time scales of interest and to eliminate any possible data processing inconsistency.

Depositing nearly all of the energy above ~100 km altitude, solar radiation at EUV wavelengths is a direct driver of density variations in the upper atmosphere. Three solar EUV proxies are examined in this work (Figure 1c), including MAVEN EUVM L2 data product for 17–22 nm (I_{MAVEN} , in units of mW/m²), extrapolated-to-Mars 10.7 cm fluxes ($F_{10.7M}$, in units of sfu) and TIMED SEE 10–100 nm fluxes (I_{TIMED} , in units of mW/m²). As shown in Figure 1c and examined in detail in the Supporting Information S1 (specifically, Figure S2), the 27-day running means of the three proxies are highly correlated with one another, having Pearson correlation coefficients as high as 0.96–0.98. Their relationships can be described by the following best-fit linear functions:

$$F_{10.7M} = 8.653 + 133.417 I_{MAVEN} \quad (1)$$

$$F_{10.7M} = 0.475 + 28.8 I_{TIMED} \quad (2)$$

$$I_{\text{TIMED}} = 0.304 + 4.534 I_{\text{MAVEN}} \quad (3)$$

Note that the data used for the correlation analysis and empirical function derivation are limited by the temporal coverage of the MAVEN data, which were collected mainly during solar minimum (see Figures 1a and 1c).

The strong correlation among the proxies suggests that any one of them is a good measure of the solar EUV heating of the upper atmosphere, despite their own advantages and disadvantages. I_{MAVEN} represents a direct measurement, but within a very narrow wavelength range. I_{TIMED} provides an estimate of solar fluxes within a broad EUV spectral interval, but is subject to extrapolation errors over a large heliocentric distance and data availability limitation from the duration of the TIMED mission. $F_{10.7M}$ represents the extrapolated solar radio flux at 10.7 cm, and is also an indirect measurement. Nevertheless, $F_{10.7}$ (or $F_{10.7M}$ after the Earth-to-Mars scaling) has long historical records and is a widely used proxy in terrestrial and planetary studies. It is $F_{10.7M}$ that Forbes et al. (2008) and Bruinsma et al. (2014) used in their long-term exospheric density variation studies. Moreover, $F_{10.7}$ is commonly adopted by terrestrial and planetary atmospheric and ionospheric models to specify solar conditions. The use of the $F_{10.7M}$ index therefore holds a particular advantage of being comparable with other observational and numerical studies. It is also beneficial as a reliable reference for future study after the end of the MAVEN and TIMED missions. Considering that $F_{10.7M}$ is reasonably accurate in the description of the long-term variation of the solar EUV flux as evidenced by the strong correlation with the other two proxies, we adopt it in this work to characterize the solar EUV driver of the Martian upper atmosphere.

Solar IR delivers another important energy source to the Martian atmosphere, through absorption by CO₂ mainly between ~50 and 120 km (Bougher & Dickinson, 1988). As a result, solar IR driving of the upper atmosphere acts primarily in an indirect manner through the upward coupling from the middle atmosphere. At the same time, solar radiation reaching Mars's orbit (regardless of irradiance wavelengths) is subject to a prominent annual variation, because the distance of Mars from the Sun significantly changes with season due to the relatively high orbital eccentricity. As shown in the SI (Figure S3 in Supporting Information S1), the seasonal dependence of the Sun-Mars distance (r_{SM} , in units of AU) and its inverse square (r_{SM}^{-2} , in units of AU⁻²) is sufficiently accurately described by the following finite cosine series:

$$\begin{aligned} r_{\text{SM}}(L_s) &\approx 1.51702 + 0.14208 \cos(L_s - 71^\circ) + 0.00672 \cos(2(L_s - 71^\circ)) \\ &\quad (\text{RMSE} : 2.01 \times 10^{-4} \text{AU}) \\ &\approx 1.51702 + 0.14208 \cos(L_s - 71^\circ) \\ &\quad (\text{RMSE} : 4.75 \times 10^{-3} \text{AU}) \end{aligned} \quad (4)$$

$$\begin{aligned} r_{\text{SM}}^{-2}(L_s) &\approx 0.44027 + 0.08193 \cos(L_s - 251^\circ) + 0.00189 \cos(2(L_s - 251^\circ)) \\ &\quad (\text{RMSE} : 5.72 \times 10^{-5} \text{AU}^{-2}) \\ &\approx 0.44027 + 0.08193 \cos(L_s - 251^\circ) \\ &\quad (\text{RMSE} : 1.33 \times 10^{-3} \text{AU}^{-2}) \end{aligned} \quad (5)$$

The root mean square errors (RMSEs) of these approximation are given after the empirical functions. r_{SM} reaches the maximum (minimum) at aphelion (perihelion) at $L_s = 71^\circ$ (251°). Solar insolation at Mars is governed by the inverse-square law by following r_{SM}^{-2} , which corresponds to a dramatic increase of 45% from aphelion to perihelion. Unlike relatively constant solar IR emissions at the Sun (e.g., Harder et al., 2009), solar EUV fluxes are highly variable in response to solar activity. Figure 1c clearly shows that solar EUV fluxes at Mars depend on solar activity by generally following the 11-year solar cycle (Figure 1a), and at the same time are also modulated by the annual cycle of the Sun-Mars distance change (Figure 1b).

Dust activity is another non-negligible contributor to atmospheric disturbances at Mars. The dust storm effects on the atmospheric thermal structure and the distributions of neutral winds and densities are well recognized in the lower and middle atmospheres, and the impact is also noticed to be extended into high altitudes in the neutral regime (thermosphere and exosphere) and in the plasma regime (ionosphere and magnetosphere) (e.g., Keating

et al., 1998; Withers & Pratt, 2013; Fang et al., 2020; Elrod et al., 2020; Lee et al., 2020; Mukundan et al., 2021). As dust particles are mostly confined below ~ 80 km altitude (Clancy et al., 2010), the dust-induced effects in the upper atmosphere act essentially indirectly through the upward coupling from the middle atmosphere (Bougher et al., 1997). However, it is unclear how long dust storms sustain their influence at high altitude, and thus whether their effects are able to show up in the climatological characteristics of the upper atmospheres. In the long-term study of Forbes et al. (2008), dust effects at 390 km, if present, would have been obscured by solar EUV effects and cannot be discerned. Bruinsma et al. (2014) noticed possible signatures of dust effects at 405 km but no apparent correlation was identified. Nevertheless, it was found in both studies that the exospheric mass density variation was very well characterized by season (L_s) and $F_{10.7M}$, without considering dust activity in their empirical models. Figure 1d describes the level of atmospheric dust loading (as a proxy of dust heating in the lower atmosphere), which is specified here as a globally averaged column dust optical depth (CDOD) at the wavelength of $9.3 \mu\text{m}$ after being scaled to the atmospheric pressure of 610 Pa (see Fang et al., 2020; Montabone et al., 2020).

3. Solar Zenith Angle Scaling

The MAVEN orbit has been designed to precess slowly in local time and latitude (see Figure 1 of Fang et al., 2021). It takes 0.21–0.30 MYs for its periapsis to complete a full precession of 24 hr of local time. About one half of its periapsis passages occurs sunward of the terminator (with solar zenith angle, SZA, varying between $\sim 8^\circ$ and 90°), with the other half tailward of the terminator (with SZA as high as $\sim 177^\circ$). Therefore, to perform a reasonable evaluation of neutral density variability, we must carefully consider the impact of SZA differences in the data.

To obtain a theoretical perspective, we utilize a time-marching run (i.e., without making steady state assumptions) of the Mars Global Ionosphere-Thermosphere Model (MGITM, Bougher et al., 2015), which was carried out by Fang et al. (2019) to investigate the 10 September 2017 ($L_s = 59^\circ$) solar flare impact in the upper atmosphere. Specifically, we adopt the 3-D model results obtained in a benchmark (nonflare) case when the solar activity was quiet. Altitude profiles that are retrieved from the model results at a SZA location at one time point are first arithmetically averaged. Repeating this step at various SZA locations allows us to reduce 3-D neutral density distributions into 2-D distributions that vary with SZA and altitude. By further averaging these 2-D maps over time within the simulated time period of about 60 Martian sols, we obtain the average SZA-altitude distributions of CO_2 , N_2 , O, and Ar, which are included in Figure S4 of the Supporting Information S1. The model results demonstrate a clear day-night asymmetry in the density distributions. The upper atmospheric densities at a given altitude tend to decrease with increasing SZA, with the decline rate significantly enhanced after crossing the terminator (particularly above ~ 200 km altitude). There are a few notable exceptions. Smooth variation with SZA is interrupted near the terminator at about 85° – 95° . Moreover, unlike the other constituents, the O density below ~ 200 km varies little or even slightly increases with SZA on the dayside, and its nightside abundance may exceed the dayside counterpart particularly below ~ 180 km. Given the complex SZA dependence of upper atmospheric density distributions on a global scale (including relatively smooth variations with SZA on the dayside and the apparent day-night asymmetry), we limit this work to analyzing the data on the dayside, specifically, $\text{SZA} \leq 80^\circ$.

The need for correcting potential biases from various SZA samplings can also be seen from MAVEN data. Figure 2 presents NGIMS CO_2 density variations within 180–185 km altitudes as a function of L_s , color coded by MY, SZA, latitude, solar EUV, and atmospheric dust loading, respectively. By generally reaching the maximum (minimum) near perihelion (aphelion), the upper thermospheric density follows a similar pattern in annual variation as what has been observed by Forbes et al. (2008) and Bruinsma et al. (2014) for the exospheric mass density. However, a striking deviation from the annual cosine curve is pronounced near about 310° – $340^\circ L_s$, where the density near $\sim 325^\circ$ is remarkably greater than nearby values by a factor of ~ 4 and is even comparable to the maximum near perihelion. As demonstrated in Figures 2a and 2c, the seeming “anomaly” occurred during the same MY of 32 and there was no dramatic shift in latitude because of slow orbital precession of MAVEN. Note that data points in Figure 2 represent the densities averaged within the 5-km altitude bin over the descending tracks orbit by orbit, and the sampled spatial position shifts westward by $\sim 60^\circ$ in longitude from one orbit to the next one due to Mars rotation. Therefore, the “anomaly” is not tied to any specific longitudes. Examination of overhead solar EUV fluxes (Figure 2d) and atmospheric dust contents (Figure 2e) reveals that these driving forces remained approximately constant within L_s of 310° – 340° . Rather, we note in Figure 2b that the density spike occurred at significantly lower SZA locations (i.e., closer to the subsolar point). The anomalously higher densities thus can be qualitatively accounted for by SZA differences according to the MGITM results discussed above.

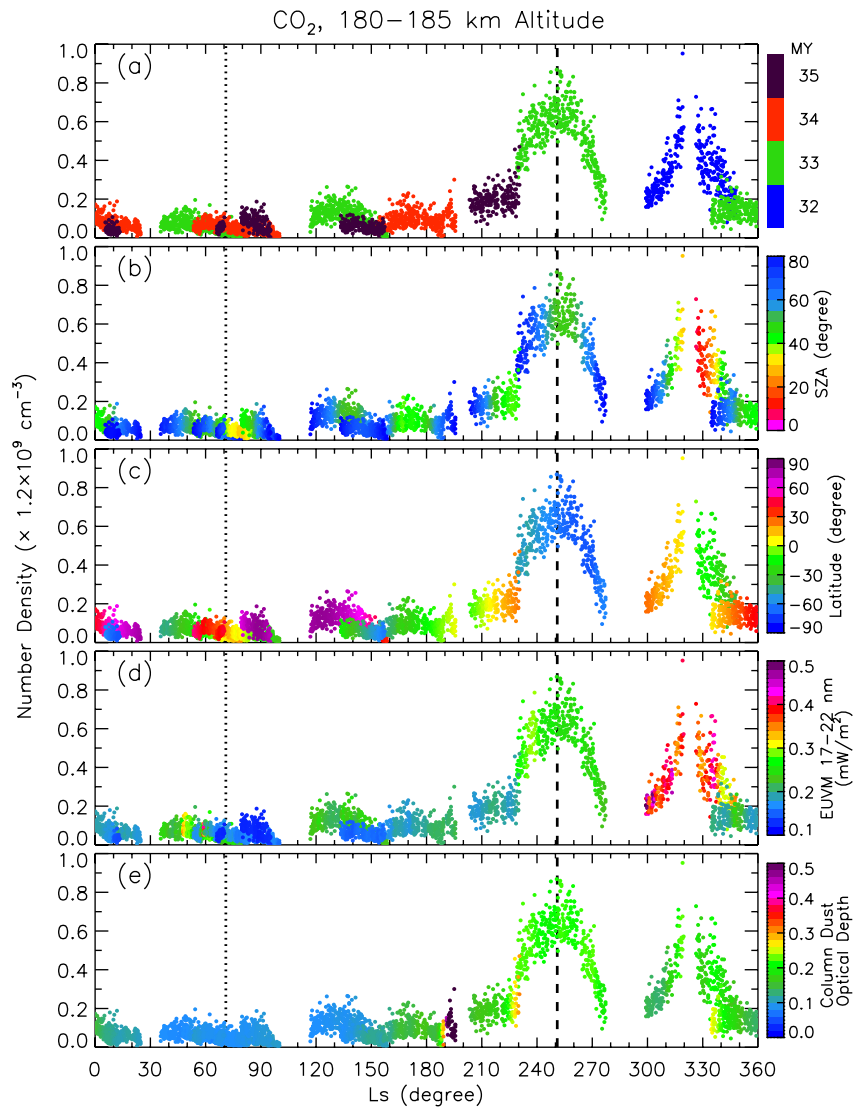


Figure 2. Mars Atmosphere and Volatile Evolution Neutral Gas and Ion Mass Spectrometer measured CO_2 density within 180–185 km altitudes on the dayside ($\text{SZA} < 80^\circ$) as a function of solar longitude, color coded by (a) Martian year, (b) SZA, (c) latitude, (d) I_{MAVEN} , and (e) globally averaged column dust optical depth. Each dot indicates the average density within the 5 km interval along the inbound orbital segments of MAVEN periapsis passages. The dotted and dashed lines mark aphelion ($L_s = 71^\circ$) and perihelion ($L_s = 251^\circ$), respectively.

In order to correct SZA biases in neutral density variations, we first use MAVEN data to statistically derive the dependence of densities with respect to SZA by assuming a linear regression equation of $n(\lambda) = f_0 + f_1\lambda$ (where n and λ denotes the neutral density and SZA, respectively). We then apply the derived relationship to scale individual measurements to a fixed baseline SZA location of 60° , which is close to the median SZA position of our adopted NGIMS dayside data sets. The scaling is performed by multiplying a data point at λ by a factor of $(f_0 + f_1 \cdot 60^\circ)/(f_0 + f_1\lambda)$. The derivation of the SZA-density relationship and the application for scaling are performed separately at different altitudes (with a 5-km resolution) and during different seasons (at a $45^\circ L_s$ interval). Figure 3 shows an example within the altitudes of 180–185 km. It is readily seen in two L_s intervals centered at 0° and 225° in this example that the densities during different MYs are very different in abundance and exhibit distinctly different slopes in their responses to SZA changes. This is expected due to the solar irradiance variation on the time scale of a solar cycle (see Figure 1a). Taking this into account, we derive and apply the SZA scaling separately for applicable combinations of altitude, L_s , and MY for each neutral species.

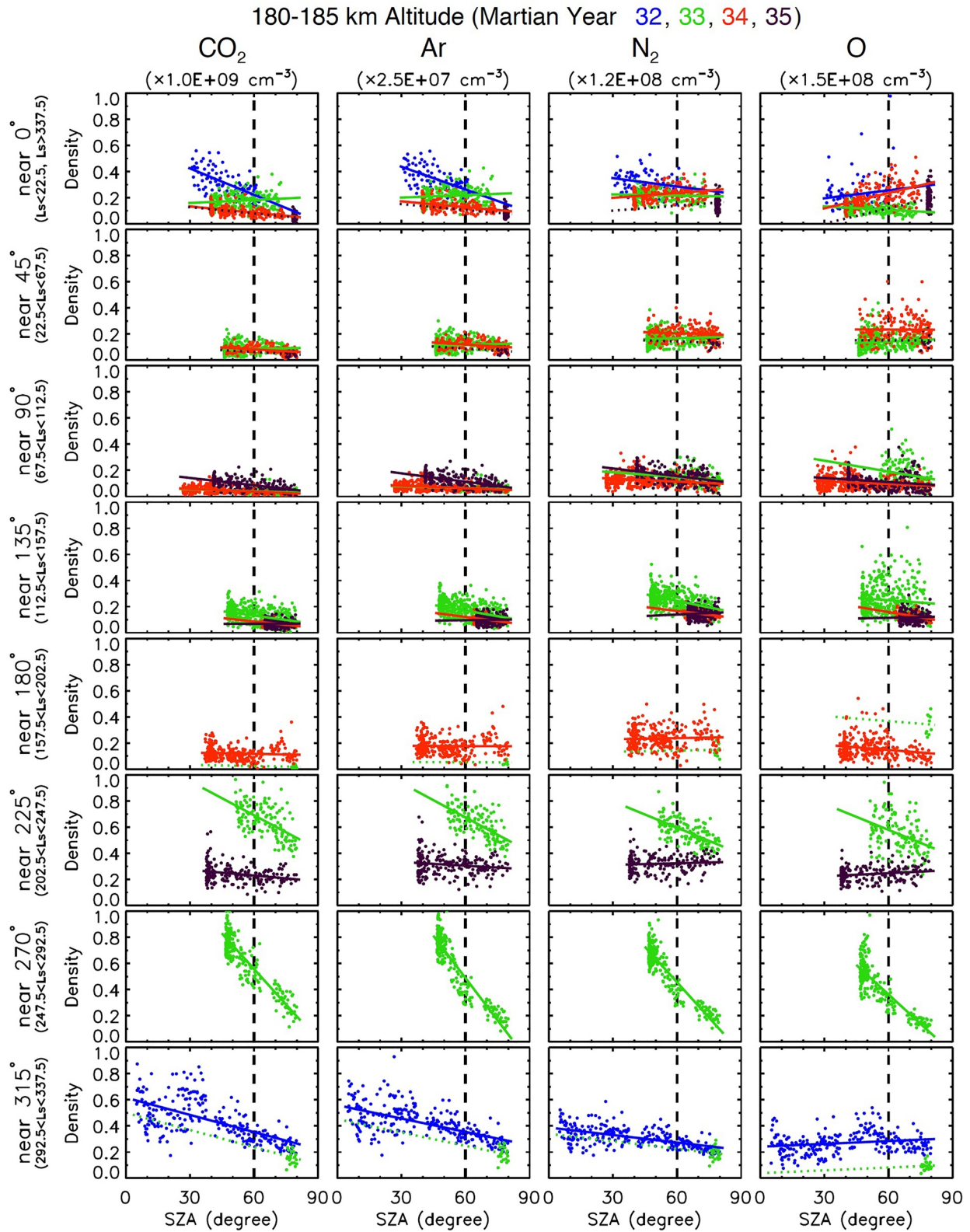


Figure 3.

As illustrated in Figure 3, the SZA variability of the neutral densities changes significantly with season, whose slope tends to be the flattest and steepest near aphelion and perihelion, respectively. In other words, the SZA scaling is most needed for the density data collected near perihelion and becomes less pressing near aphelion. The latter is also implied in Figure 2b, where the data points within L_s of 60° – 80° have comparable densities despite of their widely scattered SZA locations between 27° and 80° . The important seasonal dependence in part explains the discrepancy in the SZA variability between the MGITM prediction (as discussed above for specific $L_s = 59^\circ$, see Figure S4 of the Supporting Information S1) and the previous study of Gupta et al. (2019) (see their Figure 2). Specifically, Gupta et al. (2019) reported a relatively smooth change with SZA from the dayside to the nightside (except for He), in contrast with the abrupt change we see near the terminator from the MGITM result. We note that in the study of Gupta et al. (2019), nearly four Earth-years of MAVEN NGIMS data were averaged within SZA-altitude bins. The neglect of important density changes with season and MY (Figure 3) probably results in the fine structures that are predicted by the global model under well-constrained conditions being largely smeared out in statistical averaging.

Figure 4 shows the comparison of dayside upper thermospheric CO_2 , Ar, N_2 , and O densities within 180–185 km altitudes before and after the SZA correction. It is seen that by scaling individual data points collected under various SZAs across the dayside hemisphere to a fixed SZA location, we effectively mitigate the data bias, more apparently for CO_2 and Ar near 310° – $340^\circ L_s$ that we have seen in Figure 2. In addition, as seen from the departure from an annual harmonic fit, we note that the original densities for all the neutral species near perihelion at $\sim 275^\circ L_s$ appear unreasonably low, which is simply because the sampled regions are close to the terminator. The large enhancement after the correction is a result of the steep SZA variability near perihelion (Figure 3), but is also more subject to the uncertainty in our estimation of the SZA variability. Nevertheless, the overall remarkable improvements after the SZA scaling justify the necessity and effectiveness of the method. It should be pointed out that orbit-to-orbit variations are pronounced in data points regardless of whether the scaling is applied, which are attributed to longitudinal structures associated with atmospheric tides (e.g., Fang et al., 2021; Lo et al., 2015; Thaller et al., 2020) and/or solar EUV changes on short time scales such as minutes and hours during solar flares and solar active region evolution (see, e.g., Fang et al., 2019). Therefore, the annual harmonic fits to orbital data points in Figure 4 aim to provide a simplistic outline of the periodicity. A more statistically meaningful investigation will be made in the next section. It is worth noting in Figure 4 that MAVEN data have a nearly complete L_s coverage for the annual cycle.

4. Disentangling Orbital and Solar EUV Effects in Long-Term Variability

Figure 5 presents an overview of long-term variations of dayside upper atmospheric CO_2 , Ar, N_2 , and O densities, as a function of altitude and time. These results have been scaled to $\text{SZA} = 60^\circ$ as discussed in Section 3. The similar results without the scaling are included in Figure S5 of the Supporting Information S1 for comparison. The nearly regularly spaced data gaps are due to the precession of MAVEN periapsis into the hemisphere facing away from the Sun ($\text{SZA} > 80^\circ$). The most notable observation from Figure 5 is that the upper atmosphere undergoes periodic expansion and contraction. On average, there is an apparent annual tendency for atmospheric columns to rise to a higher altitude near perihelion and descend back near aphelion. A detailed examination of the altitudes where these atmospheric species have a density of 10^7 cm^{-3} (as an example) confirms that their 27-day averaged values follow a prominent annual cycle with fluctuations of about 20–30 km in altitude (see Figure S6 in the Supporting Information S1). In addition, a close look at Figure 5 shows that there is a severe lack of MAVEN NGIMS coverage during high dust activity in the dayside upper atmosphere. In particular, during the 2018 planet-encircling dust storm (which is the only global dust storm since the launch of the MAVEN mission), the periapsis of the spacecraft was initially near the terminator and then precessed into the nightside, thus unfortunately missing the observation of atmospheric responses on the dayside. Furthermore, the side-by-side comparison in Figure 5a illustrates that the occurrence of high atmospheric dust loading generally coincides with enhanced solar EUV fluxes at the Mars's orbit and/or peak r_{SM}^{-2} at perihelion. This constitutes a particular challenge to

Figure 3. (left to right) Dayside atmospheric CO_2 , Ar, N_2 , and O densities within 180–185 km altitudes as a function of SZA within eight $45^\circ L_s$ intervals centered from (top) $0^\circ L_s$ to (bottom) $315^\circ L_s$. The densities have been normalized by constant values as marked at the top of the panels. The colors of data points indicate different MYs: blue for MY32, green for MY33, red for MY34, and dark purple for MY35. Linear regression of densities versus SZA is performed separately for different MYs and is superposed as solid lines. In case that data points in one MY span less than 10° in SZA, we use the slope from the other MY that has the maximum SZA coverage as an approximation. These approximated SZA dependence is marked in dotted line, as seen near L_s of 180° and 315° for MY33, and near 0° and 45° for MY35. The black vertical dashed line denotes the position of $\text{SZA} = 60^\circ$.

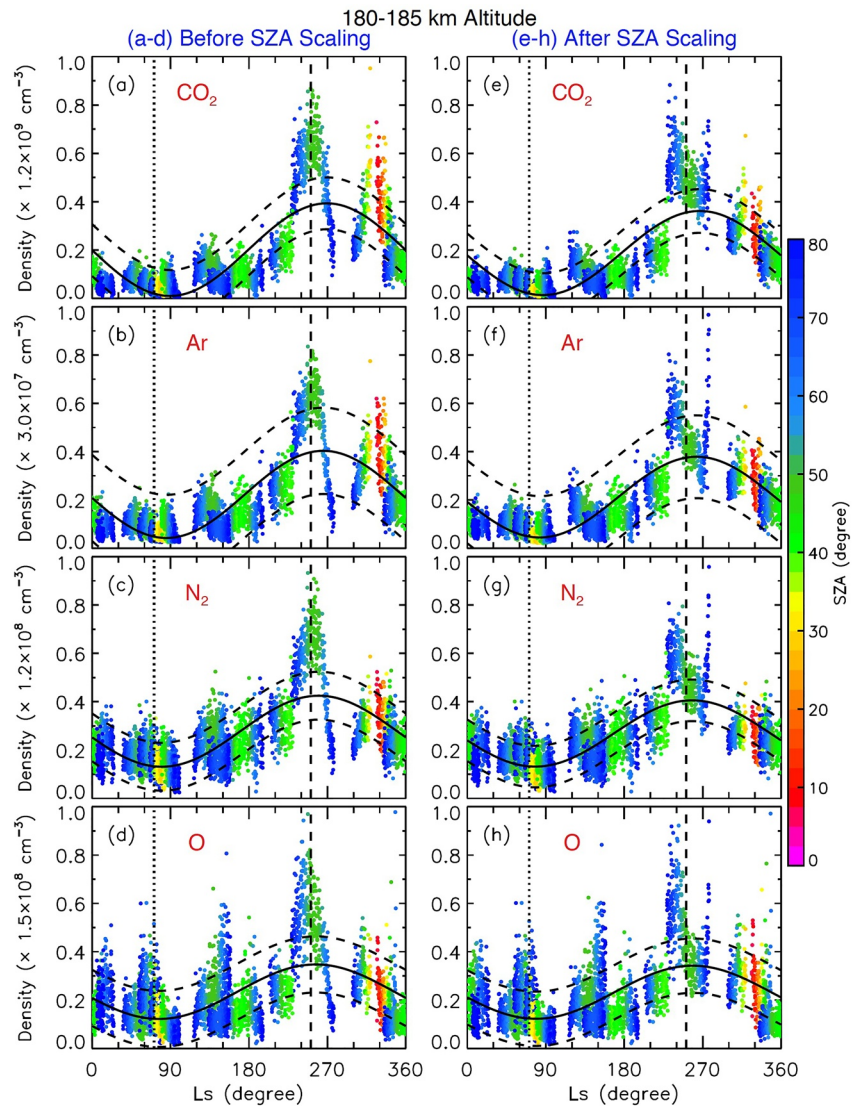


Figure 4. Comparison of (top to bottom) dayside atmospheric CO₂, Ar, N₂, and O densities within 180–185 km altitudes as a function of L_s , before and after SZA scaling. The left column shows the results from the original NGIMS data, and the right column shows the results after individual data points have been scaled to a fixed baseline SZA location of 60°. The thick solid curves represent a fit with an annual harmonic cycle, and the dashed curves are one-sigma uncertainties. The vertical dotted and dashed lines mark aphelion and perihelion, respectively. Panel (a) is reproduced from Figure 2b.

disentangle dust storm effects from the other drivers, as also noticed by Forbes et al. (2008). Considering all of these together, we exclude dust storm effects from our current long-term variability analysis in order to avoid inappropriate interpretation in the absence of sufficient high-dust-activity coverage. As will be shown later, this neglect is not problematic. Actually, the MAVEN data during the onset of the 2018 dust storm are included and show no particular density perturbations (Figure 2e).

Following Forbes et al. (2008), Krasnopolsky (2010), and Bruinsma et al. (2014), we start with the investigation of how upper atmospheric densities vary in response to the orbital eccentricity of Mars and solar EUV changes at the top of the atmosphere. The former determines the annual variation of the Sun-Mars distance and thus modulates solar irradiance through the inverse square of the distance. We use r_{SM}^{-2} to measure this driving factor and term it the orbital effect. For the latter, as elaborated in Section 2, we select 10.7-cm radio fluxes scaled from Earth to Mars ($F_{10.7M}$) as the proxy. Therefore, we conduct multiple linear regression fits by assuming

$$n_s = n_{s0} + n_{s1} r_{SM}^{-2} + n_{s2} F_{10.7M} \quad (6)$$

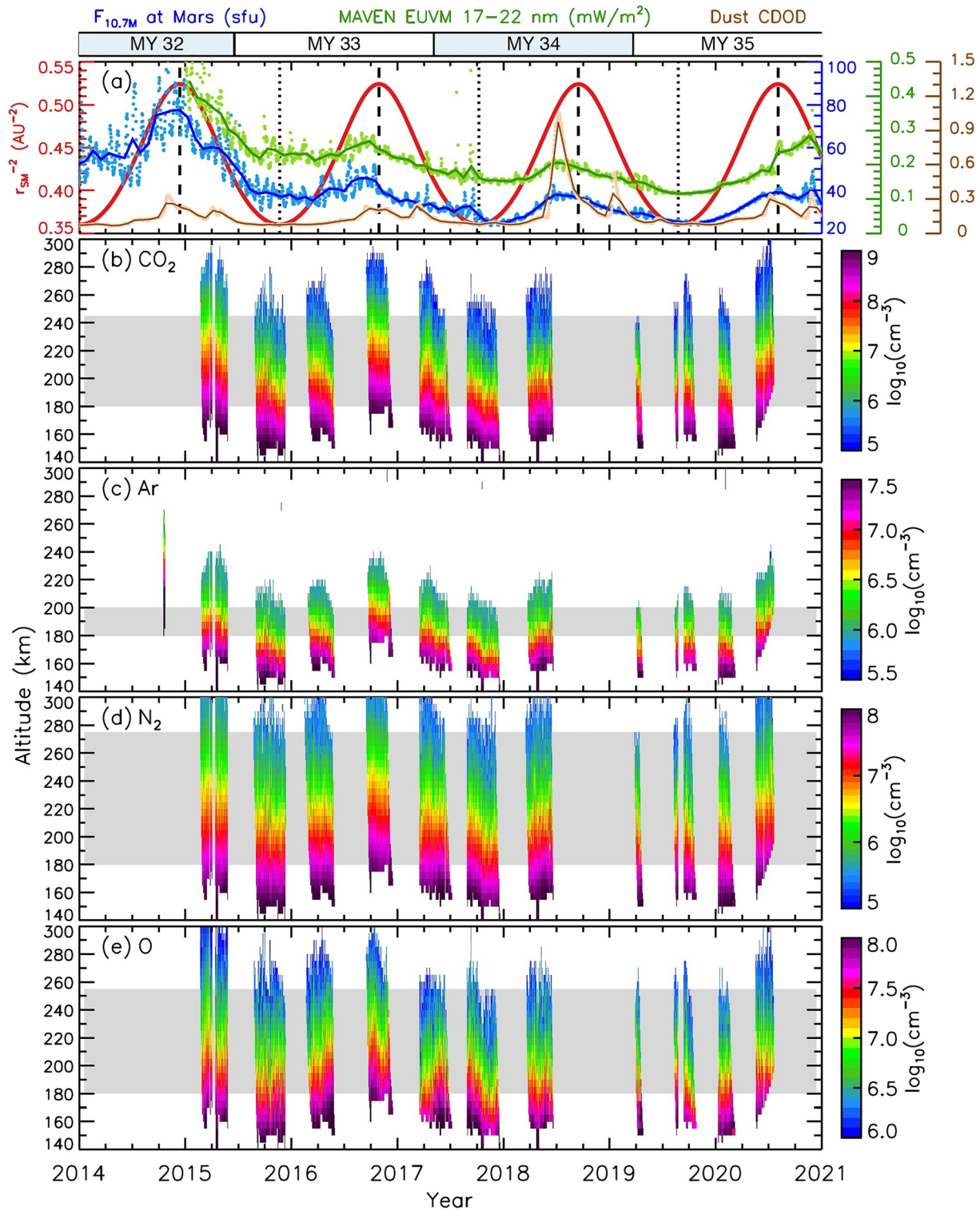


Figure 5. Panel (a) shows the inverse square of the Sun-Mars distance (r_{SM}^{-2} , red, left vertical axis), solar extreme ultraviolet proxies at Mars ($F_{10.7M}$ and I_{MAVEN} in blue and green, respectively, right vertical axes), and globally averaged atmospheric dust loading (brown, right vertical axis). These information, which is similar to what has been included in Figure 1, provides the long-term variability of driving factors for the upper atmosphere. The dotted and dashed lines mark aphelion and perihelion, respectively. Panels (b-e) present Neutral Gas and Ion Mass Spectrometer (NGIMS) CO₂, Ar, N₂, and O densities averaged at 5-km altitude intervals along Mars Atmosphere and Volatile Evolution (MAVEN) inbound orbital segments on the dayside (SZA < 80°). These densities have been scaled to SZA = 60°. The horizontal gray shadings mark the altitude ranges over which the long-term variability of the densities is analyzed.

where n_s is the average upper atmospheric density at SZA = 60° within a 5-km altitude bin. The subscript “s” denotes the neutral species of CO₂, Ar, N₂, or O. The fitting parameters of n_{sk} ($k = 0, 1, 2$) are constants, depending on neutral species and altitude. The last two terms on the right side of Equation 6 describe the orbital and solar EUV effects, respectively.

The use of $F_{10.7M}$ (instead of $F_{10.7}$ at Earth) in Equation 6 has several noteworthy advantages. First and most importantly, it facilitates our understanding of how the Martian upper atmosphere responds to the driving of the overhead solar radiation. Solar IR is the main solar energy input to the middle atmosphere (e.g., Bougher & Dickinson, 1988). Its intensity at the Sun, with a variation many orders of magnitude smaller than neutral density variations that we have seen, is reasonably regarded as a constant (e.g., Harder et al., 2009). Therefore, the term of r_{SM}^{-2} differs from solar IR fluxes at the top of the Martian atmosphere by only a constant multiplication factor. On the other hand, $F_{10.7M}$ directly describes the solar EUV intensity at the top of the atmosphere. Because its energy is completely absorbed in the upper atmosphere, the solar EUV effect represents the direct control of downward-directed solar irradiance. Therefore, a multiple linear regression for examining the relationship of atmospheric densities with overhead solar IR and solar EUV intensities would be readily transformed to Equation 6. This is the main reason why we choose Equation 6 (in particular, using $F_{10.7M}$ rather than $F_{10.7}$) to explore the relative importance of the incident solar irradiance over different wavelength ranges. Although both of the solar IR and EUV terms are subject to the r_{SM} modulation, they represent essentially independent driving forces to the Martian atmosphere. The correlation between the solar IR and EUV terms does not represent a physical connection between them, and will be carefully handled using a statistically robust method to retrieve their relative importance to density distributions. Second, our analysis using $F_{10.7M}$ is in line with the works of Forbes et al. (2008), Krasnopolsky (2010), and Bruinsma et al. (2014). This consistency facilitates a direct comparison of our findings with previous studies, which will be shown in Section 5.

There are a few points worth noting here. First, as the MAVEN periapsis continuously and slowly precesses in local time and latitude, we study dayside hemispheric responses as a whole with the north-south asymmetry neglected. In other words, even though the L_s dependence has been implicitly included in the orbital effect through Equation 5, we neglect the differences in atmospheric densities between summer and winter hemispheres due to the tilt of the planet's rotational axis. Second, the early works of Forbes et al. (2008), Krasnopolsky (2010), and Bruinsma et al. (2014) used cosine functions of L_s to characterize annual variations in their empirical models. As implied by the relatively low-order approximation in Equation 5 (which actually provides sufficiently accurate results), their cosine terms are essentially a linear function of r_{SM}^{-2} , if we further neglect the small difference in their phase terms with respect to L_s . For instance, the term of $-4.5 \cos(L_s - 72^\circ)$ in Equation 1 of Forbes et al. (2008) is close to $4.5 \cos(L_s - 251^\circ)$ and thus transformed to $-24.182 + 54.925 r_{SM}^{-2}$. From this perspective, our use of r_{SM}^{-2} factor works in a similar way as the previously adopted cosine functions of L_s . More importantly, r_{SM}^{-2} straightforwardly points to the annual variation due to the Sun-Mars distance change. Third, rather than nonlinearly combining the orbital and solar EUV effects in the long-term density variability as in Krasnopolsky (2010) and Bruinsma et al. (2014), we adopt the classic multiple linear regression (which essentially is adopted by Forbes et al. [2008]). The purpose is (a) to avoid overfitting in empirical formula derivation and (b) to ease quantification and interpretation of relative contributions of the driving factors (which will be discussed later).

In addition, as discussed in Section 3, there is a strong orbit-to-orbit variability in atmospheric densities. In order to remove interference of the orbital variability from long-term variabilities, we calculate 27-day averaged values of atmospheric densities and the two driving factors (i.e., r_{SM}^{-2} and $F_{10.7M}$) and then conduct multiple linear regressions among them. The 27-day averaging time window is commensurate with the nominal solar rotation period, allowing us to minimize influence from solar active region evolution on solar irradiance (mainly on solar EUV) and on solar wind properties, the latter of which are speculated by Bruinsma et al. (2014) to have an impact on exospheric densities. Moreover, 27-day averaging mitigates wave forcing effects by equivalently computing zonal means of longitudinal structures associated with tidal oscillations. As demonstrated by Thaller et al. (2020) and Fang et al. (2021), 2–3 weeks of MAVEN data are good enough for a well-spread longitude sampling thanks to the ~4.5-hr or shorter orbital periodicity. In other words, 27-day averaging is necessary and adequate to remove short spatial and temporal variations from long-term variations. Furthermore, we ensure the same seasonal coverage at different altitudes for appropriate altitude comparison. As marked by the gray shadings in Figure 5, we perform the long-term variability analysis within limited altitude ranges at 5-km intervals: 180–245 km for CO₂, 180–200 km for Ar, 180–275 km for N₂, and 180–255 km for O.

Figure 6 shows the multiple linear regression fit (black curves) within 180–185 km altitudes as an example. The coefficient of determination (R^2), or the square of the multiple correlation coefficient (R), provides a measure of the proportion of the variance in a dependent variable (i.e., atmospheric densities in our case) that can be explained by multiple predictors (i.e., r_{SM}^{-2} and $F_{10.7M}$). The calculated R^2 values are labeled as the total contributions on the right side of the panels. It is found that 68%–75% of CO_2 , Ar, and N_2 density variances near 180 km can be accounted for by variations in r_{SM}^{-2} and $F_{10.7M}$. In contrast, R^2 is significantly low at the level of $\sim 50\%$ for the density of O. The red and blue curves in Figure 6 show the partial variations determined by the orbital term ($n_{s1} r_{SM}^{-2}$) and the solar EUV term ($n_{s2} F_{10.7M}$), respectively, which have been shifted downward by their minimum values for the demonstration purpose so that the adjusted minima of the both curves are the same (i.e., zero). It is readily illustrated that the red curves predominate over the blue curves and thus constitute the major part of the long-term variability at the examined altitude. For atmospheric O, its red curve still exceeds the blue curve, although they are close to being comparable. It is suggested that upper thermospheric densities near 180 km are primarily controlled by the orbital effect and secondarily modulated by solar EUV.

It is of interest to notice large scatter in the MAVEN data near $L_s = 225^\circ$ in MY33 (Figure 3) and the corresponding departure of our multiple linear regression fit (Figure 6). As seen from Figure 6b, this time period corresponds to MAVEN's periapsis being at high latitudes in the southern hemisphere. The polar regions are natural settings for increased variability due to the sharp gradients that exist in connection with tides and planetary waves that must satisfy continuity constraints at the poles (see, e.g., Forbes et al., 2020). During MY33, this variability at high latitudes during southern hemisphere summer was compounded by the effects of a regional dust storm that occurred (Wu et al., 2020). The dust height, opacity and associated temperature response due to solar heating increased precipitously close to $L_s = 225^\circ$ at 62.5°S . The increased heating likely generated vertically propagating solar tides directly, and indirectly through wave-wave interactions (e.g., Forbes et al., 2020), that propagated into the thermosphere and carried with them the day-to-day and longitudinal variability of the lower-atmosphere forcing. The density scatter results in a short-term departure from the long-term variability and probably also affects our SZA scaling of the densities.

Although the comparison of the red and blue curves as demonstrated in Figure 6 is helpful for visual examination, we are unable to quantify the density variability by them. We still need a statistically robust approach to partition the relative contributions of the orbital and solar EUV effects in density variations. For this purpose, however, the commonly used zero-order Pearson correlation does not work. While it measures the direct predictive ability of a predictor, it does not consider the contributions from other predictors. As a consequence, the sum of the squared zero-order correlations over all predictors is typically not equal to R^2 , except when predictors are mutually uncorrelated. The exception is not applicable to the current study, as $F_{10.7M}$ depends on both solar activity and the Sun-Mars distance. For this work, we adopt a widely accepted statistical method called Dominance Analysis (DA; Azen & Budescu, 2003; Budescu, 1993). DA determines the relative importance of predictors in multiple regression, by calculating the average increase in R^2 resulting from adding a predictor to all possible sub-models through pairwise comparisons. Its noteworthy features include the consideration of correlations between predictors and the fact that the derived contributions over all predictors sum up to R^2 . See the Supporting Information S1 for a brief description of the DA approach.

We extend the multiple linear regression analysis as shown in Figure 6 for 180–185 km altitude to up to 275 km (as highlighted by horizontal gray shadings in Figure 5). Within each altitude bin, we calculate the proportion of the density variance that can be explained by the combined effects (i.e., R^2) of r_{SM}^{-2} and $F_{10.7M}$, and then apply the DA method to further partition it into the individual contributions between the orbital and solar EUV effects. The fitting results and the derived contributions are listed in Table 1, and are also displayed in Figure 7 for an examination of their altitude dependence. The individual and combined contributions are expressed in units of percent.

Figure 7 shows that upper atmospheric densities above 180 km can be reasonably well predicted by the inverse square of the Sun-Mars distance and the solar EUV intensity at Mars. The multiple correlation coefficients are sufficiently high such that the combination of the orbital and solar EUV effects is able to account for $\sim 70\%$ – 85% of density variances of CO_2 , N_2 , and Ar. While the altitude coverage of Ar is significantly limited, the available comparison as given in Figure 7 suggests that Ar behaves similarly to CO_2 and N_2 . The chemically active species of atmospheric O, however, behaves distinctly differently from the other species: the two drivers of r_{SM}^{-2} and $F_{10.7M}$ together account for only about 50%–70% of oxygen density variations. It is worth noting that the uncertainty error bars on NGIMS CO_2 and O 'IV' data are the same, which are dominated by counting statistics uncertainties.

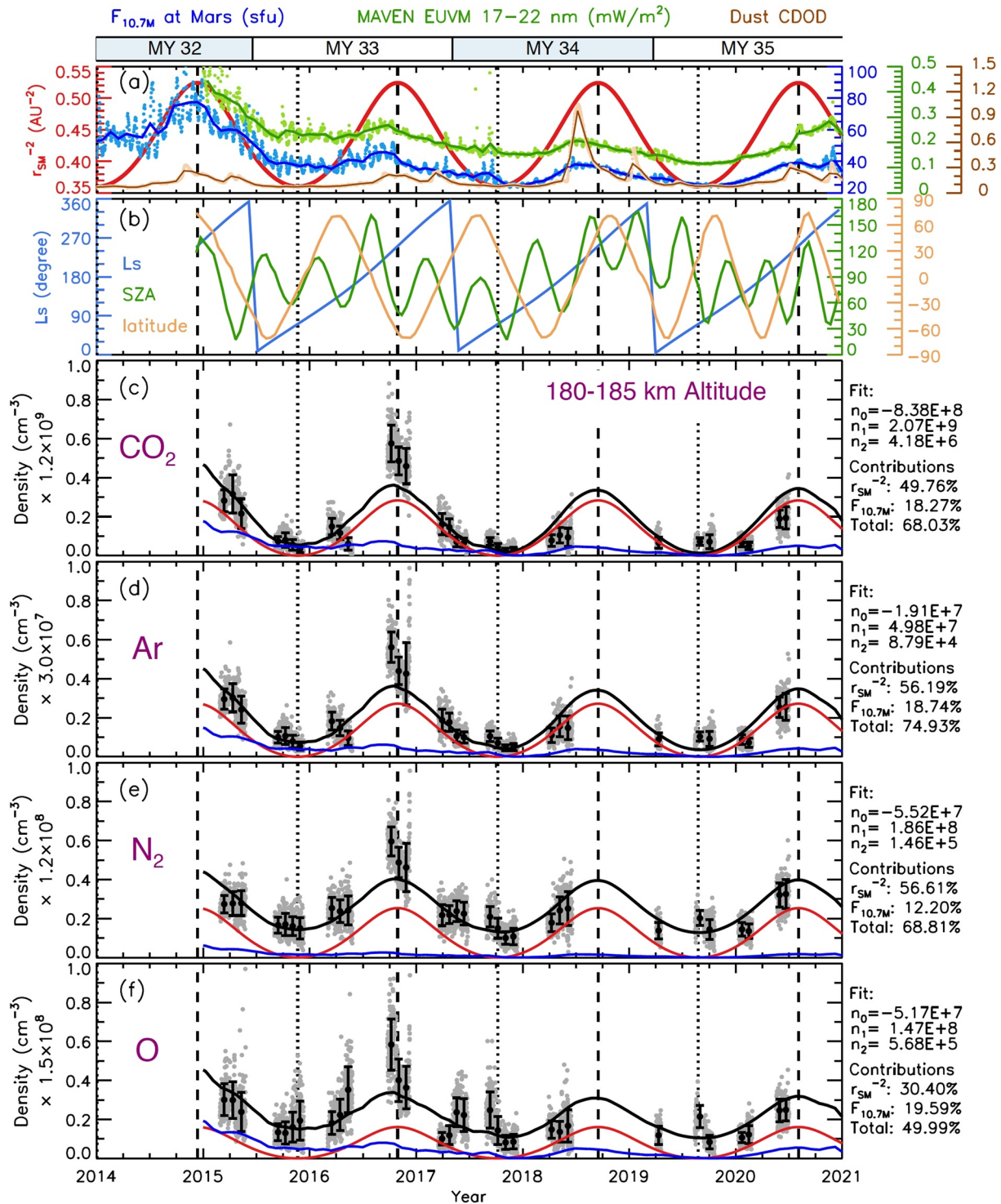


Figure 6. Panel (a) is the same as in Figure 5. Panel (b) shows Mars Atmosphere and Volatile Evolution (MAVEN) periapsis locations: Ls (left vertical axis, in blue), SZA (right vertical axis, in green), and latitude (right vertical axis, in orange). Panels (c–f) show the temporal variations of NGIMS CO_2 , Ar, N_2 , and O densities within 180–185 km altitudes on the dayside. The gray dots indicate the average values of SZA-scaled densities within the altitude bin along MAVEN inbound orbital segments. The black dots represent the 27-day averaged densities and the error bars correspond to standard deviations. The 27-day averaged values of densities, r_{SM}^{-2} , and $F_{10.7M}$ are used to construct multiple linear regressions in the form of $n = n_0 + n_1 r_{SM}^{-2} + n_2 F_{10.7M}$, which are shown as black curves. The red and blue curves show the results from $n_1 r_{SM}^{-2}$ and $n_2 F_{10.7M}$, respectively, but shifted by constant values so that their minima are zero. The fitting parameters as well as the contributions by the orbital and solar extreme ultraviolet (EUV) effects (see the text) are labeled on the right side of the panels. The vertical dotted and dashed lines mark aphelion and perihelion, respectively.

Table 1

Multiple Linear Regression for Dayside Upper Atmospheric CO₂, N₂, O, and Ar Densities at 60° SZA and Percentage Contributions of the Orbital and Solar EUV Effects to Density Variances

Altitude (km)	CO ₂						N ₂					
	<i>n</i> ₀ ^a	<i>n</i> ₁ ^a	<i>n</i> ₂ ^a	<i>D</i> _{orb} ^b	<i>D</i> _{EUV} ^b	<i>D</i> _{tot} ^b	<i>n</i> ₀	<i>n</i> ₁	<i>n</i> ₂	<i>D</i> _{orb}	<i>D</i> _{EUV}	<i>D</i> _{tot}
270–275	–	–	–	–	–	–	–7.97(5)	1.88(6)	1.21(4)	40.9	43.2	84.1
265–270	–	–	–	–	–	–	–1.16(6)	2.75(6)	1.39(4)	46.2	38.6	84.8
260–265	–	–	–	–	–	–	–1.59(6)	3.80(6)	1.64(4)	49.3	35.4	84.8
255–260	–	–	–	–	–	–	–2.09(6)	5.02(6)	1.97(4)	50.4	33.2	83.6
250–255	–	–	–	–	–	–	–2.75(6)	6.64(6)	2.39(4)	52.3	31.7	84.1
245–250	–	–	–	–	–	–	–3.52(6)	8.56(6)	2.84(4)	53.6	30.2	83.8
240–245	–6.35(6) ^c	1.16(7)	8.96(4)	36.0	44.8	80.7	–4.45(6)	1.10(7)	3.40(4)	54.4	28.9	83.4
235–240	–1.03(7)	2.01(7)	1.25(5)	39.6	39.9	79.4	–5.60(6)	1.41(7)	3.93(4)	56.1	27.1	83.2
230–235	–1.65(7)	3.40(7)	1.72(5)	42.8	35.5	78.3	–6.95(6)	1.79(7)	4.55(4)	57.2	25.6	82.8
225–230	–2.58(7)	5.50(7)	2.43(5)	44.7	32.7	77.4	–8.68(6)	2.27(7)	5.40(4)	57.6	24.5	82.1
220–225	–3.98(7)	8.73(7)	3.39(5)	46.6	30.2	76.8	–1.07(7)	2.86(7)	6.37(4)	58.0	23.5	81.5
215–220	–6.00(7)	1.33(8)	4.85(5)	47.8	29.4	77.1	–1.32(7)	3.54(7)	7.92(4)	57.0	23.2	80.2
210–215	–8.88(7)	2.01(8)	6.71(5)	49.2	27.9	77.1	–1.60(7)	4.42(7)	9.13(4)	57.4	21.9	79.3
205–210	–1.30(8)	2.98(8)	9.09(5)	50.2	26.1	76.3	–1.95(7)	5.55(7)	1.01(5)	57.7	19.9	77.6
200–205	–1.87(8)	4.36(8)	1.23(6)	50.9	24.7	75.6	–2.38(7)	6.98(7)	1.15(5)	57.8	18.6	76.3
195–200	–2.69(8)	6.38(8)	1.64(6)	51.5	23.1	74.6	–2.87(7)	8.76(7)	1.23(5)	57.7	16.8	74.5
190–195	–3.85(8)	9.26(8)	2.26(6)	50.0	21.4	71.4	–3.51(7)	1.11(8)	1.31(5)	57.3	15.1	72.4
185–190	–5.63(8)	1.38(9)	3.00(6)	50.3	19.7	70.0	–4.38(7)	1.44(8)	1.32(5)	58.1	13.4	71.5
180–185	–8.38(8)	2.07(9)	4.18(6)	49.8	18.3	68.0	–5.52(7)	1.86(8)	1.46(5)	56.6	12.2	68.8
Altitude (km)	O						Ar					
	<i>n</i> ₀	<i>n</i> ₁	<i>n</i> ₂	<i>D</i> _{orb}	<i>D</i> _{EUV}	<i>D</i> _{tot}	<i>n</i> ₀	<i>n</i> ₁	<i>n</i> ₂	<i>D</i> _{orb}	<i>D</i> _{EUV}	<i>D</i> _{tot}
250–255	–1.94 (6)	5.56(6)	5.23(4)	28.2	42.4	70.7	–	–	–	–	–	–
245–250	–2.41(6)	6.27(6)	6.55(4)	25.8	42.8	68.6	–	–	–	–	–	–
240–245	–3.34(6)	8.13(6)	7.94(4)	26.7	41.6	68.3	–	–	–	–	–	–
235–240	–4.72(6)	1.08(7)	9.84(4)	28.3	41.4	69.7	–	–	–	–	–	–
230–235	–6.16(6)	1.40(7)	1.17(5)	29.6	39.9	69.5	–	–	–	–	–	–
225–230	–7.92(6)	1.78(7)	1.40(5)	30.2	38.6	68.7	–	–	–	–	–	–
220–225	–9.76(6)	2.24(7)	1.63(5)	30.7	36.3	67.0	–	–	–	–	–	–
215–220	–1.20(7)	2.74(7)	1.96(5)	30.0	35.3	65.3	–	–	–	–	–	–
210–215	–1.44(7)	3.34(7)	2.33(5)	29.4	33.7	63.1	–	–	–	–	–	–
205–210	–1.69(7)	4.07(7)	2.67(5)	29.0	31.5	60.5	–	–	–	–	–	–
200–205	–2.06(7)	5.11(7)	3.12(5)	29.4	29.6	59.0	–	–	–	–	–	–
195–200	–2.50(7)	6.46(7)	3.59(5)	29.2	26.8	56.0	–6.23(6)	1.61(7)	3.58(4)	56.4	22.4	78.8
190–195	–3.11(7)	8.35(7)	4.15(5)	29.6	24.3	53.9	–9.13(6)	2.33(7)	5.01(4)	55.6	21.5	77.1
185–190	–3.92(7)	1.09(8)	4.84(5)	30.0	22.1	52.2	–1.32(7)	3.41(7)	6.55(4)	56.5	20.1	76.6
180–185	–5.17(7)	1.47(8)	5.68(5)	30.4	19.6	50.0	–1.91(7)	4.98(7)	8.79(4)	56.2	18.7	74.9

^a*n*₀, *n*₁, and *n*₂ are the fitting parameters in Equation 6 in units of cm^{–3}, cm^{–3}AU², and cm^{–3}sfu^{–1}. ^b*D*_{orb} and *D*_{EUV} represent the percentage contributions of the orbital and solar EUV effects to density variances calculated using Dominance Analysis. *D*_{tot} is the total contribution: *D*_{tot} = *D*_{orb} + *D*_{EUV}. ^cNumbers in parenthesis denote powers of 10. For instance, –6.35 (6) denotes –6.35 × 10⁶.

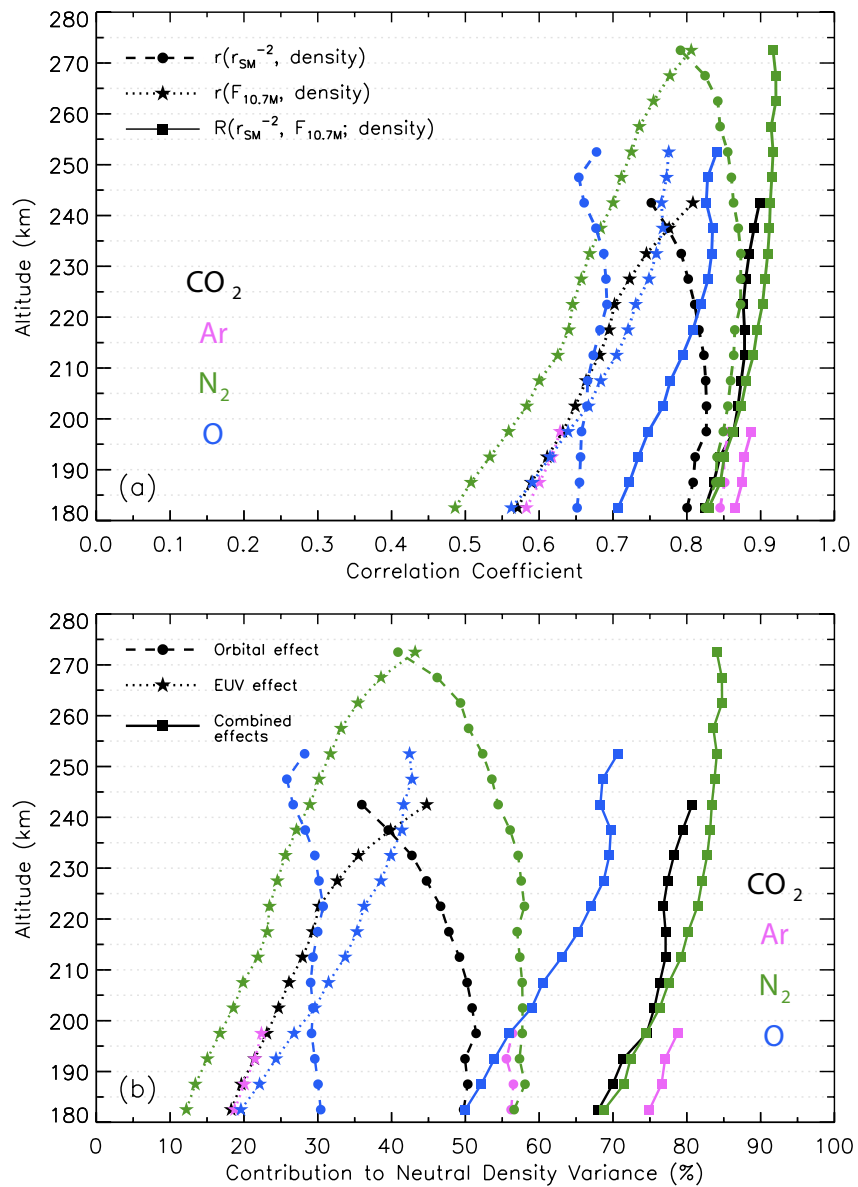


Figure 7. Panel (a) shows the altitude profiles of Pearson's zero-order correlation coefficients between atmospheric densities and r_{SM}^{-2} (dashed lines with circles) and $F_{10.7M}$ (dotted line with stars). The multiple correlation coefficients (R) are shown as solid lines with squares. Panel (b) shows the percentage contributions of r_{SM}^{-2} and $F_{10.7M}$ to atmospheric density variances calculated using Dominance Analysis, and their total contributions (which are equal to R^2) are also shown. Different colors represent different atmospheric species: CO₂ (black), Ar (magenta), N₂ (green), and O (blue).

Regardless of the atmospheric constituents, the combined r_{SM}^{-2} and $F_{10.7M}$ effects quickly increase with altitude until reaching ~210–230 km, above which they remain relatively constant (at least up to 280 km).

The partitioning of the orbital and solar EUV effects represents the first attempt to quantify the relative importance of both drivers in controlling upper atmospheric densities. It is illustrated in Figure 7b that the contribution of the orbital effect is relatively constant in the upper thermosphere and lower exosphere at the level of ~50% for CO₂, ~60% for N₂ and Ar, and ~30% for O, and then a rapid drop starts above ~210 km for CO₂ and ~230 km for N₂ and O. It is interesting to note that the orbital effect in O appears to reverse the decrease near ~245 km and is slightly strengthened above. On the other hand, the solar EUV effect makes a modest contribution to density variances at 180 km of order 20% for CO₂, Ar, and O, and ~10% for N₂. It then steadily increases with rising altitude for all the neutral species. For CO₂ and N₂, the solar EUV effect increases more rapidly with altitude

starting from ~ 225 km and ~ 260 km, respectively. In contrast, the solar EUV effect in atmospheric O increases at a slower rate near ~ 230 km and exhibits a slight decreasing tendency above ~ 245 km. Although the insufficient MAVEN data coverage at higher altitudes prevents us from statistically investigating the further variation there, the comparison with the MGS data near 400 km (which will be discussed in the next section) implies that the tendency change near ~ 245 km for atmospheric O is probably real. In addition, an extrapolation to altitudes below 180 km following the derived trends implies that the solar EUV effect becomes insignificant for all of the neutral species below 150 km altitude. This is consistent with the fact that solar EUV heating of the atmosphere is concentrated at high altitudes and rapidly decreases below ~ 160 km (e.g., Bougher & Dickinson, 1988). Additional support comes from a numerical study of dayside atmospheric disturbances during one of the most powerful solar flare events (X8.2-class) on 10 September 2017 (Fang et al., 2019). Based on global, time-dependent simulations using MGITM, it is found that although the neutral temperature is enhanced down to about 110 km altitude resulting from solar radiation enhancement particularly over X-ray and EUV wavelengths, important disturbances in neutral densities (in association with atmospheric upwelling driven by solar EUV heating) are essentially concentrated above 150 km.

A key observation of Figure 7b is that the relative importance of the orbital and solar EUV effects dynamically varies with altitude. The orbital effect dominates the neutral density variation in the upper thermosphere over the solar EUV effect. However, they follow opposite trends with altitude. The orbital effect remains basically constant at low altitudes and then quickly declines with altitude. This is in contrast to the tendency of a continuous increase with altitude for the solar EUV effect. As a result, these two effects cross at high altitudes and are of comparable importance in determining neutral density structures. The transition region is in the lower exosphere and is located approximately at 240 km, 270 km, and 205 km for CO_2 , N_2 , and O, respectively. Above the transition altitude, the solar EUV effect exceeds the orbital effect and becomes the primary driver in regulating atmospheric densities. The altitude variation of the relative importance of the orbital and solar EUV effects sheds light on the competition of the controlling effects of solar radiation over different wavelength ranges within different atmospheric layers. The competition of the orbital and solar EUV effects as revealed in Figure 7 is indicative of the competition in the upper atmosphere between the indirect effect of solar IR and the direct effect of solar EUV. It is thus not surprising to see that the indirect effect in the upper atmosphere via the upward coupling from the middle atmosphere declines gradually with altitude. As shown in Figure 7, the indirect orbital effect is eventually overtaken by the direct solar EUV effect at high altitudes away from the low-altitude IR energy absorption region.

5. Discussion and Solar Cycle Variations

The analysis of long-term variability has been limited to below 275 km altitude due to the limitation of the MAVEN NGIMS data coverage (Figure 5). Nevertheless, the long-term MGS and MO POD data sets (Figure 1e) are valuable for extending the investigation to about 400 km altitude. Moreover, the fact that the MAVEN data are collected basically during solar minimum and the MGS and MO data span a complete solar cycle enables not only the exploration of the vertical variation of the orbital and solar EUV effects between 275 and 400 km under solar minimum conditions, but also examination of the solar cycle impact near 400 km. In addition, the MGS and MO data were obtained at high latitudes in the southern hemisphere near afternoon local times, with SZA close to 60° (Bruinsma et al., 2014; Krasnopolsky, 2010). The similarity of the SZA locations makes a comparison between MAVEN and MGS/MO data appropriate.

Figure 8a shows the long-term variation derived from MAVEN O densities at the highest available 250–255 km altitude bin, and its comparison with previous predictions from Equation 1 of Forbes et al. (2008) and Equation 5 of Krasnopolsky (2010) at 390 km and from Equation 2 of Bruinsma et al. (2014) at 405 km. The comparison of these long-term variations shows a general consistency, exhibiting prominent annual cycles and additional modulation by solar EUV. A few notes are worth mentioning. First, the constant term in Equation 1 of Forbes et al. (2008) has been corrected to have a negative sign, which was pointed out by Krasnopolsky (2010) and has been confirmed by our examination (not shown here). The resulting negative mass densities near aphelion draw attention to the caveat of applying the empirical function obtained under solar maximum conditions to solar minimum. Second, the MAVEN results are obtained from O densities near 255 km while the previous results are from MGS and MO POD-derived atmospheric mass densities near 400 km. The exosphere at 400 km is predominately atomic oxygen (Mahaffy, Benna, Elrod, et al., 2015), although sometimes helium is non-negligible particularly due to the winter helium bulge (Bruinsma et al., 2014). With the altitude and potential compositional differences

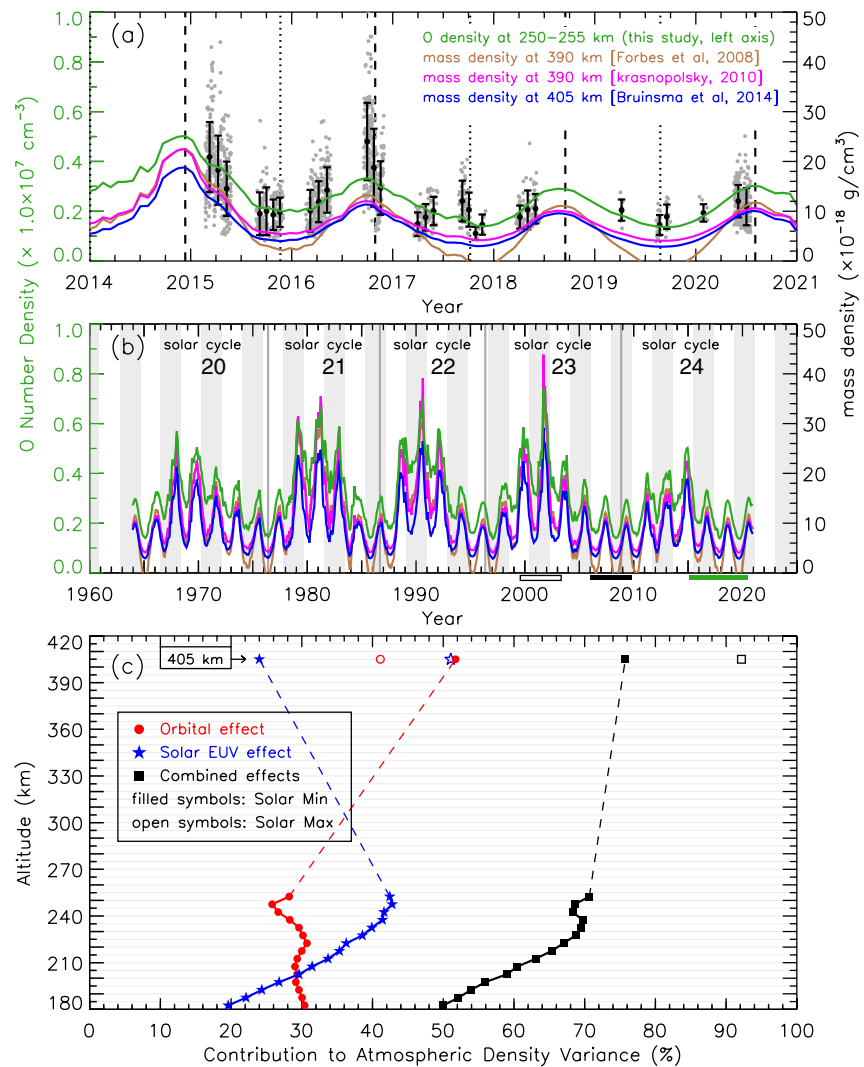


Figure 8. Comparison of long-term variability including and the orbital and solar extreme ultraviolet (EUV) effects from Mars Atmosphere and Volatile Evolution (MAVEN) O densities with those from MGS and Mars Odyssey (MO) Precise Orbit Determination (POD)-estimated exospheric mass densities. In panel (a), the gray and black dots and the error bars are similar to those in Figure 6f but within 250–255 km altitudes (left vertical axis). The multiple linear regression results are shown as the green curve. The curves in other colors represent previous empirical model predictions near 400 km as marked (right vertical axis). Panel (b) is similar to panel (a) but extends the long-term variability comparisons to the last 5 solar cycles. Panel (c) compares the orbital contribution (red circles), solar EUV contribution (blue stars), and total contribution (black squares) using MAVEN measured O densities below 255 km and MGS and MO POD-estimated mass densities at 405 km. The contributions at 405 km are derived separately under the conditions of solar minimum (similar to MAVEN observational conditions, shown as filled symbols) and solar maximum (open symbols). The corresponding time periods are highlighted by the filled and open horizontal bars in black below the X axis of panel (b), respectively. The green horizontal bar marks the time span of the MAVEN data. The dashed lines in panel (c) outline the potential connection between 255 and 405 km altitudes during solar minimum.

in mind, the overall consistency is also well maintained over the last 5 solar cycles as demonstrated in Figure 8b. It is important to note the apparent annual and solar cycle variations, which underscore the driving of r_{SM}^{-2} and $F_{10.7M}$ in the upper atmosphere.

We then apply the DA procedure to evaluate the relative importance of the orbital and solar EUV effects near 400 km, using the MGS and MO combined POD data sets that are directly retrieved from Figure 3 of Bruinsma et al. (2014). To distinguish the solar cycle impact, we extract two full MYs of data subsets during solar maximum and minimum phases, which are marked below the horizontal axis of Figure 8b by open and filled horizontal bars

(in black), respectively. As seen from Figure 1e, these subsets of solar maximum and minimum data essentially are taken from MGS and MO POD data, respectively. The DA-derived contributions of the orbital and solar EUV effects at 405 km during the two representative solar cycle phases are presented in Figure 8c, in comparison with lower-altitude MAVEN results that are obtained during solar minimum.

It is illustrated in Figure 8c that during solar minimum, the solar EUV effect in atmospheric O densities nearly monotonically increases with rising altitude from 20% at 180 km to 42% at 255 km (also see Table 1), above which the growth is disrupted. The analysis of the MO data at 405 km reveals a significantly reduced solar EUV contribution of 24% at solar minimum, implying a decrease of the effect within regions between 255 and 405 km. This drop is consistent with the reduction of atmospheric absorption of solar EUV at high altitudes. In contrast, the orbital effect is relative constant at low altitudes at the level of $\sim 30\%$ and then undergoes a modest decrease starting from ~ 230 km until reaching ~ 245 km, above which an increase must have happened such that the orbital contribution is more than doubled from 28% at 255 km to 52% at 405 km. Furthermore, the combination of the orbital and solar EUV effects during solar minimum accounts for 50% of atmospheric O density variances at 180 km, increasing to 71% at 255 km, and slightly to 76% at 405 km. As a result, during solar minimum, the variation of O density in the lower exosphere is primarily caused by the variation of the incoming solar EUV flux. At 405 km where the atmospheric absorption of solar EUV becomes insignificant, the exospheric density varies mainly with the Sun-Mars distance, suggesting that the change of solar IR heating in the middle atmosphere extends high into the exosphere.

To our knowledge, the physical origins of middle-atmosphere solar IR driving of upper atmosphere variability have not been specifically addressed in the literature, and would require modeling to provide definitive interpretation. It is also possible that shortwave insolation absorption by dust and other heating mechanisms below 50 km could be contributing. It seems plausible, though, that the thermosphere response is transmitted through the hydrostatic law vis-a-vis changes in thermal structure, and possibly modulation of the meridional circulation that manifests in minor constituents such as O. It should be pointed out that our use of the term “solar IR” in this study is a catch-all, in that effects due to other heating in the lower atmosphere may in principle lumped into what we are calling the “solar IR” response.

The comparison at 405 km in Figure 8c also shows the solar cycle variation in the relative importance of the orbital and solar EUV effects. From solar minimum to maximum, the orbital effect decreases from 52% to 41% and the solar EUV effect considerably increases from 24% to 51%, resulting in a great increase from 76% to 92% for their combined contributions to exospheric density variances. The enhanced solar EUV effect can be explained by the increase of the atmospheric absorption of solar EUV at high altitudes, which is attributed to a denser and more expanded atmosphere on average during solar maximum. The variation of atmospheric expansion with the solar cycle is readily demonstrated in Figure 8b. Given that the large-scale vertical shift of the atmosphere is rooted in the middle atmosphere due to solar IR heating, the fact that the atmospheric expansion is visible at 405 km is a clear indication that the orbital effect reaches high into the exosphere. This explains that the orbital effect is always a key driver at 405 km regardless of the solar cycle phase, even though its relative importance may be surpassed by the solar EUV effect during solar maximum.

Unlike 92% of exospheric density variations at 405 km that can be reasonably attributed to the changes of r_{SM}^{-2} and $F_{10.7M}$ during solar maximum, this number is significantly reduced to 76% during solar minimum. It suggests that the importance of other factors than the Sun-Mars distance and solar EUV changes from negligible to significant in correspondence with the solar cycle change from maximum to minimum. Candidate factors include atmospheric dust loading and tilt of the planet's rotational axis (or the seasonal effect), which are not considered in the current work. Nevertheless, the examination of Figure 7b shows that during solar minimum, unconsidered factors become important for atmospheric O but not that important for atmospheric species of CO_2 , N_2 , and Ar on a long time scale. Moreover, the impact of unconsidered factors decreases with increasing altitude, considering that the combined orbital and solar EUV effects increase with altitude. It is reasonably speculated that the unconsidered but sometimes significant factors most likely originate at low altitudes with their relative importance decreasing with altitude. We note that the regression fit by Bruinsma et al. (2014) produces a reasonably good agreement with the MGS and MO POD data during solar maximum but shows a significant departure during solar minimum. This is consistent with our finding that r_{SM}^{-2} and $F_{10.7M}$ are indeed major drivers but other effects play an increasing role during low solar activity.

6. Summary and Conclusions

Observations of the Martian upper atmosphere (above ~ 100 km altitude) have been especially scarce. In particular, atmospheric density distributions at altitudes higher than ~ 200 km were hardly measured prior to the MAVEN mission. Due to the limitation of sparse and disparate data sets collected in the pre-MAVEN era, climatological characteristics and variability of the upper atmosphere are unavailable, except for a handful of previous studies in which exospheric mass density variations were evaluated using MGS and MO POD data near 400 km altitude.

In this study, we make use of nearly three MYs of in-situ measurements by the NGIMS instrument along the inbound orbital segments of MAVEN periapsis passages. Due to the dynamic change of the spacecraft periapsis altitude, the temporal coverage is optimal above 180 km, and below 245, 275, 200, and 255 km for atmospheric species of CO_2 , N_2 , Ar, and O, respectively. In order to retrieve atmospheric density changes caused by external driving factors instead of spatial differences in sampling, we focus our statistical analysis on the dayside upper atmosphere ($\text{SZA} \leq 80^\circ$). This is to take advantage of relatively smooth variations of dayside atmospheric densities with SZA and to avoid uncertainties resulting from the strong day-night asymmetry, given that the MAVEN periapsis continuously precesses in local time and latitude. In order to further minimize the potential bias due to various SZA samplings, we derive the average SZA dependence separately for applicable combinations of altitude, L_s , and MY for each neutral species, which is then applied to scale individual data points to $\text{SZA} = 60^\circ$ (which is close to the median SZA location of the data). The results confirm the effectiveness of the SZA scaling, which is most (least) needed for the density data collected near perihelion (aphelion). In order to remove perturbations from solar rotational effects and tide-induced longitudinal structures, we further make 27-day averages at 5-km altitude intervals for the SZA-scaled dayside atmospheric densities.

Long-term variations of the average CO_2 , N_2 , O, and Ar densities in the upper atmosphere are analyzed during the time period of 2015–2020, which corresponds to low solar activity. The variability is evaluated using multiple linear regression of the densities to the inverse square of the Sun-Mars distance and the solar EUV intensity at the top of the atmosphere. The former (r_{SM}^{-2}) essentially describes the solar IR intensity at Mars. Solar IR is sufficiently constant at the Sun and its flux reaching the planet varies annually due to the orbital eccentricity of Mars. For solar EUV, we select the 10.7-cm radio flux ($F_{10.7\text{M}}$) that has been extrapolated from Earth to Mars. Although other EUV proxies (including MAVEN EUVM directly measured 17–22 nm fluxes and TIMED SEE derived 10–100 nm fluxes) are available and strongly correlated with each other, we select $F_{10.7\text{M}}$ by considering the availability of its long historical records and the ease of comparison with existing and future observational and modeling studies. Because solar IR and EUV deposit their energies in different atmospheric regions, the orbital and solar EUV effects within the upper atmosphere represent the driving of solar irradiance indirectly through the upward coupling from the middle atmosphere and directly through atmospheric absorption, respectively. Using the coefficient of determination (R^2), we calculate the proportion of density variances that can be explained by the combination of the orbital and solar EUV effects. Since r_{SM}^{-2} and $F_{10.7\text{M}}$ are partially correlated via the Sun-Mars distance, their squared zero-order correlation coefficients with densities do not sum up to R^2 and thus cannot be used to indicate the relative importance of the driving factors. To resolve this challenge, we apply the statistical method of Dominance Analysis to partition R^2 into individual contributions between the orbital and solar EUV effects. This is the first time that the relative importance of the orbital and solar EUV effects on CO_2 , N_2 , O, and Ar densities versus altitude (180–275 km) are quantified, compared, and interpreted.

In addition, we make use of a solar cycle's worth of MGS and MO POD data at 405 km that have been compiled by Forbes et al. (2008) and Bruinsma et al. (2014). Specifically, we extract two full MYs of data subsets during solar minimum and maximum phases and apply the DA procedure to disentangle the orbital and solar EUV effects for intercomparison between low and high solar activities and also for comparison with MAVEN results at low solar activity.

Our findings are summarized as follows.

1. The upper atmosphere undergoes periodic expansion and contraction on an annual basis. Upper atmospheric densities tend to minimize near aphelion and maximize near perihelion, on top of which they are also modulated by solar EUV fluxes
2. The combination of the orbital effect (proportional to r_{SM}^{-2}) and the solar EUV effect (proportional to $F_{10.7\text{M}}$) accounts for a majority of variances in atmospheric CO_2 , N_2 , and Ar densities by $\sim 70\%$ – 85% and in atmospheric O densities by $\sim 50\%$ – 70% . The combined effects quickly increase with altitude until reaching ~ 210 –

230 km, above which they remain relatively constant. It is implied that other driving factors that are not included in this study (e.g., dust storms, seasonal effects due to the tilt of the planet's rotational axis) play a minor role in affecting CO₂, N₂, and Ar densities. The relatively large unexplained fraction of O density variances is partly due to the unconsidered factors and partly to complex chemical and transport processes for this chemically active species

3. The orbital effect is relatively constant in the upper thermosphere and lower exosphere at the level of ~50% for CO₂, ~60% for N₂ and Ar, and ~30% for O. It decreases with rising altitude above ~210 km for CO₂ and ~230 km for N₂ and O. The solar EUV effect at 180 km altitude has a level of ~20% for CO₂, Ar, and O, and of ~10% for N₂, and then nearly monotonically increases as altitude increases. The downward extrapolation of the solar EUV effect into lower altitudes implies that it is negligible below ~150 km
4. The orbital effect and solar EUV effect are comparable at approximately 240 km, 270 km, and 205 km for CO₂, N₂, and O, respectively. That is, the orbital (solar EUV) effect plays a predominant role in affecting density distributions below (above) these transition altitudes. The orbital effect reflects the indirect control by solar IR via the upward coupling from the middle atmosphere, whose relative importance decreases with altitude away from solar IR absorption regions. On the other hand, as solar EUV is absorbed along its downward penetration and almost completely in the upper atmosphere, solar EUV has a direct impact on atmospheric densities. The competition between these two effects shows that the indirect solar IR control is more important in the lower part of the upper atmosphere but is overtaken at higher altitudes by the direct solar EUV control
5. We compare the variances of MAVEN-measured O densities below 255 km and MGS and MO POD-estimated mass densities at 405 km during solar minimum. It is found that the fraction of the density variance accountable for by the solar EUV effect decreases from 42% at 255 km to 24% at 405 km, in comparison with the increase of the orbital effect from 28% to 52%. It is implied that at 405 km where the atmospheric absorption of solar EUV is less significant during low solar activity, the variability in the exospheric density is primarily caused by the Sun-Mars distance change on an annual basis
6. At 405 km altitude, from solar minimum to solar maximum, the orbital effect decreases from 52% to 41% and the solar EUV effect increases considerably from 24% to 51%, resulting in a great increase from 76% to 92% for their combined contributions to exospheric density variances. It is shown that the orbital effect is always a key driver at 405 km regardless of the solar cycle phase. While the solar EUV effect plays a minor role at 405 km during solar minimum, it is greatly enhanced during high solar activity and slightly exceeds the orbital effect

Data Availability Statement

The MAVEN data are publicly available at NASA Planetary Data System through https://pds-atmospheres.nmsu.edu/data_and_services/atmospheres_data/MAVEN/ngims.html. The column dust optical depth is obtained through the Mars Climate Database project at http://www-mars.lmd.jussieu.fr/mars/dust_climatology/index.html. The sunspot number and $F_{10.7}$ are obtained from the OMNI database at <https://omniweb.gsfc.nasa.gov/form/dx3.html>. The TIMED/SEE solar radiation data are obtained from <https://lasp.colorado.edu/home/see/data/>. The results from this study are available at <https://scholar.colorado.edu/concern/datasets/5x21tg60v>.

References

- Azen, R., & Budescu, D. V. (2003). The dominance analysis approach for comparing predictors in multiple regression. *Psychological Methods*, 8(2), 129–148. <https://doi.org/10.1037/1082-989X.8.2.129>
- Bougher, S., & Dickinson, R. (1988). Mars mesosphere and thermosphere: 1. Global mean heat budget and thermal structure. *Journal of Geophysical Research: Space Physics*, 93(A7), 7325–7337. <https://doi.org/10.1029/ja093ia07p07325>
- Bougher, S., Murphy, J., & Haberle, R. (1997). Dust storm impacts on the Mars upper atmosphere. *Advances in Space Research*, 19(8), 1255–1260. [https://doi.org/10.1016/S0273-1177\(97\)00278-0](https://doi.org/10.1016/S0273-1177(97)00278-0)
- Bougher, S., Pawlowski, D., Bell, J., Nelli, S., McDunn, T., Murphy, J., et al. (2015). Mars global ionosphere-thermosphere model: Solar cycle, seasonal, and diurnal variations of the Mars upper atmosphere. *Journal of Geophysical Research: Planets*, 120(2), 311–342. <https://doi.org/10.1002/2014JE004715>
- Bruinsma, S., Forbes, J. M., Marty, J.-C., Zhang, X., & Smith, M. D. (2014). Long-term variability of Mars' exosphere based on precise orbital analysis of Mars global surveyor and Mars odyssey. *Journal of Geophysical Research: Planets*, 119(1), 210–218. <https://doi.org/10.1002/2013JE004491>
- Budescu, D. V. (1993). Dominance analysis: A new approach to the problem of relative importance of predictors in multiple regression. *Psychological Bulletin*, 114(3), 542. <https://doi.org/10.1037/0033-2909.114.3.542>

Acknowledgments

This work was supported by NASA grant 80NSSC19K0562 (XF), NASA grant 80NSSC21K1821 (JMF), NASA grant 80GSFC21M0002 (MB) and the NASA MAVEN project through the Mars Exploration Program.

- Clancy, R. T., Wolff, M. J., Whitney, B. A., Cantor, B. A., Smith, M. D., & McConnochie, T. H. (2010). Extension of atmospheric dust loading to high altitudes during the 2001 Mars dust storm: Mgs tes limb observations. *Icarus*, 207(1), 98–109. <https://doi.org/10.1016/j.icarus.2009.10.011>
- Elrod, M. K., Bougher, S. W., Roeten, K., Sharrar, R., & Murphy, J. (2020). Structural and compositional changes in the upper atmosphere related to the pede-2018 dust event on Mars as observed by maven ngims. *Geophysical Research Letters*, 47(4), e2019GL084378. <https://doi.org/10.1029/2019GL084378>
- Eparvier, F., Chamberlin, P., Woods, T., & Thiemann, E. (2015). The solar extreme ultraviolet monitor for maven. *Space Science Reviews*, 195(1), 293–301. <https://doi.org/10.1007/s11214-015-0195-2>
- Fang, X., Forbes, J. M., Gan, Q., Liu, G., Thaller, S., Bougher, S., et al. (2021). Tidal effects on the longitudinal structures of the martian thermosphere and topside ionosphere observed by maven. *Journal of Geophysical Research: Space Physics*, 126(2), e2020JA028562. <https://doi.org/10.1029/2020JA028562>
- Fang, X., Ma, Y., Lee, Y., Bougher, S., Liu, G., Benna, M., et al. (2020). Mars dust storm effects in the ionosphere and magnetosphere and implications for atmospheric carbon loss. *Journal of Geophysical Research: Space Physics*, 125. <https://doi.org/10.1029/2019JA026838>
- Fang, X., Ma, Y., Masunaga, K., Dong, Y., Brain, D., Halekas, J., et al. (2017). The Mars crustal magnetic field control of plasma boundary locations and atmospheric loss: Mhd prediction and comparison with maven. *Journal of Geophysical Research: Space Physics*, 122(4), 4117–4137. <https://doi.org/10.1002/2016JA023509>
- Fang, X., Pawlowski, D., Ma, Y., Bougher, S., Thiemann, E., Eparvier, F., et al. (2019). Mars upper atmospheric responses to the 10 September 2017 solar flare: A global, time-dependent simulation. *Geophysical Research Letters*, 46(16), 9334–9343. <https://doi.org/10.1029/2019GL084515>
- Forbes, J. M., Lemoine, F. G., Bruinsma, S. L., Smith, M. D., & Zhang, X. (2008). Solar flux variability of Mars' exosphere densities and temperatures. *Geophysical Research Letters*, 35(1). <https://doi.org/10.1029/2007GL031904>
- Forbes, J. M., Zhang, X., Forget, F., Millour, E., & Kleinböhl, A. (2020). Solar tides in the middle and upper atmosphere of Mars. *Journal of Geophysical Research: Space Physics*, 125(9), e2020JA028140. <https://doi.org/10.1029/2020JA028140>
- Forget, F., Montmessin, F., Bertaux, J.-L., González-Galindo, F., Lebonnois, S., Quemerais, E., et al. (2009). Density and temperatures of the upper martian atmosphere measured by stellar occultations with Mars express spicam. *Journal of Geophysical Research: Planets*, 114(E1). <https://doi.org/10.1029/2008JE003086>
- Gupta, N., Venkateswara Rao, N., & Kadhane, U. R. (2019). Dawn-dusk asymmetries in the martian upper atmosphere. *Journal of Geophysical Research: Planets*, 124(12), 3219–3230. <https://doi.org/10.1029/2019JE006151>
- Harder, J. W., Fontenla, J. M., Pilewskie, P., Richard, E. C., & Woods, T. N. (2009). Trends in solar spectral irradiance variability in the visible and infrared. *Geophysical Research Letters*, 36(7). <https://doi.org/10.1029/2008GL036797>
- Jakosky, B. M., Brain, D., Chaffin, M., Curry, S., Deighan, J., Grebowsky, J., et al. (2018). Loss of the martian atmosphere to space: Present-day loss rates determined from maven observations and integrated loss through time. *Icarus*, 315, 146–157. <https://doi.org/10.1016/j.icarus.2018.05.030>
- Jakosky, B. M., Lin, R. P., Grebowsky, J. M., Luhmann, J. G., Mitchell, D., Beutelschies, G., et al. (2015). The Mars atmosphere and volatile evolution (maven) mission. *Space Science Reviews*, 195(1), 3–48. <https://doi.org/10.1007/s11214-015-0139-x>
- Keating, G., Bougher, S., Zurek, R., Tolson, R., Cancro, G., Noll, S., et al. (1998). The structure of the upper atmosphere of Mars: In situ accelerometer measurements from Mars global surveyor. *Science*, 279(5357), 1672–1676. <https://doi.org/10.1126/science.279.5357.1672>
- Krasnopolsky, V. A. (2010). Solar activity variations of thermospheric temperatures on Mars and a problem of co in the lower atmosphere. *Icarus*, 207(2), 638–647. <https://doi.org/10.1016/j.icarus.2009.12.036>
- Lee, Y., Fang, X., Gacesa, M., Ma, Y., Tenishev, V., Mahaffy, P., et al. (2020). Effects of global and regional dust storms on the martian hot corona and photochemical loss. *Journal of Geophysical Research: Space Physics*, 125(4), e2019JA027115. <https://doi.org/10.1029/2019JA027115>
- Lo, D. Y., Yelle, R. V., Schneider, N. M., Jain, S. K., Stewart, A. I. F., England, S. L., et al. (2015). Nonmigrating tides in the martian atmosphere as observed by maven iuv. *Geophysical Research Letters*, 42(21), 9057–9063. <https://doi.org/10.1002/2015GL066268>
- Mahaffy, P. R., Benna, M., Elrod, M., Yelle, R. V., Bougher, S. W., Stone, S. W., & Jakosky, B. M. (2015). Structure and composition of the neutral upper atmosphere of Mars from the maven ngims investigation. *Geophysical Research Letters*, 42(21), 8951–8957. <https://doi.org/10.1002/2015GL065329>
- Mahaffy, P. R., Benna, M., King, T., Harpold, D. N., Arvey, R., Barciniak, M., et al. (2015). The neutral gas and ion mass spectrometer on the Mars atmosphere and volatile evolution mission. *Space Science Reviews*, 195(1), 49–73. <https://doi.org/10.1007/s11214-014-0091-1>
- Montabone, L., Spiga, A., Kass, D. M., Kleinböhl, A., Forget, F., & Millour, E. (2020). Martian year 34 column dust climatology from Mars climate sounder observations: Reconstructed maps and model simulations. *Journal of Geophysical Research: Planets*. <https://doi.org/10.1029/2019JE006111>
- Mukundan, V., Thampi, S. V., Bhardwaj, A., & Fang, X. (2021). Impact of the 2018 Mars global dust storm on the ionospheric peak: A study using a photochemical model. *Journal of Geophysical Research: Planets*, 126(4), e2021JE006823. <https://doi.org/10.1029/2021JE006823>
- Nier, A., & McElroy, M. (1976). Structure of the neutral upper atmosphere of Mars: Results from viking 1 and viking 2. *Science*, 194(4271), 1298–1300. <https://doi.org/10.1126/science.194.4271.1298>
- Schofield, J., Barnes, J. R., Crisp, D., Haberle, R. M., Larsen, S., Magalhaes, J., et al. (1997). The Mars pathfinder atmospheric structure investigation/meteorology (asi/met) experiment. *Science*, 278(5344), 1752–1758. <https://doi.org/10.1126/science.278.5344.1752>
- Siddle, A., Mueller-Wodarg, I., Bruinsma, S., & Marty, J.-C. (2021). Density structures in the martian lower thermosphere as inferred by trace gas orbiter accelerometer measurements. *Icarus*, 357, 114109. <https://doi.org/10.1016/j.icarus.2020.114109>
- Thaller, S. A., Andersson, L., Pilinski, M. D., Thiemann, E., Withers, P., Elrod, M., et al. (2020). Tidal wave-driven variability in the Mars ionosphere-thermosphere system. *Atmosphere*, 11(5), 521. <https://doi.org/10.3390/atmos11050521>
- Tolson, R., Bemis, E., Hough, S., Zaleski, K., Keating, G., Shidner, J., et al. (2008). Atmospheric modeling using accelerometer data during Mars reconnaissance orbiter aerobraking operations. *Journal of Spacecraft and Rockets*, 45(3), 511–518. <https://doi.org/10.2514/1.34301>
- Tolson, R., Dwyer, A., Hanna, J., Keating, G., George, B., Escalera, P., & Werner, M. (2005). Application of accelerometer data to Mars odyssey aerobraking and atmospheric modeling. *Journal of Spacecraft and Rockets*, 42(3), 435–443. <https://doi.org/10.2514/1.15173>
- Wilson, R. J. (2002). Evidence for nonmigrating thermal tides in the Mars upper atmosphere from the Mars global surveyor accelerometer experiment. *Geophysical Research Letters*, 29(7), 24–31. <https://doi.org/10.1029/2001GL013975>
- Withers, P., & Pratt, R. (2013). An observational study of the response of the upper atmosphere of Mars to lower atmospheric dust storms. *Icarus*, 225(1), 378–389. <https://doi.org/10.1016/j.icarus.2013.02.032>
- Woods, T. N., Eparvier, F. G., Bailey, S. M., Chamberlin, P. C., Lean, J., Rottman, G. J., et al. (2005). Solar EUV experiment (see): Mission overview and first results. *Journal of Geophysical Research: Space Physics*, 110(A1). <https://doi.org/10.1029/2004JA010765>
- Wu, Z., Li, T., Zhang, X., Li, J., & Cui, J. (2020). Dust tides and rapid meridional motions in the martian atmosphere during major dust storms. *Nature Communications*, 11(1), 1–10. <https://doi.org/10.1038/s41467-020-14510-x>

- Yoshida, N., Nakagawa, H., Terada, N., Evans, J., Schneider, N., Jain, S., et al. (2020). Seasonal and latitudinal variations of dayside n₂/co₂ ratio in the martian thermosphere derived from maven iuvs observations. *Journal of Geophysical Research: Planets*, *125*(12), e2020JE006378. <https://doi.org/10.1029/2020JE006378>
- Zurek, R., Tolson, R., Bougher, S., Lugo, R., Baird, D., Bell, J., & Jakosky, B. (2017). Mars thermosphere as seen in maven accelerometer data. *Journal of Geophysical Research: Space Physics*, *122*(3), 3798–3814. <https://doi.org/10.1002/2016JA023641>